International Journal of Fracture **74:** 289–324, 1996.

Numerical simulations of dynamic crack growth along an interface

X.-P. XU[1] and A. NEEDLEMAN[2]
[1]*Materials Department, College of Engineering, University of California, Santa Barbara, CA 93106, USA*
[2]*Division of Engineering, Brown University, Providence, Rhode Island 02912, USA*

Received 7 October 1994; accepted in revised form 22 May 1995

Abstract. Dynamic crack growth is analyzed numerically for a plane strain bimaterial block with an initial central crack. The material on each side of the bond line is characterized by an isotropic hyperelastic constitutive relation. A cohesive surface constitutive relation is also specified that relates the tractions and displacement jumps across the bond line and that allows for the creation of new free surface. The resistance to crack initiation and the crack speed history are predicted without invoking any *ad hoc* failure criterion. Full finite strain transient analyses are carried out, with two types of loading considered; tensile loading on one side of the specimen and crack face loading. The crack speed history and the evolution of the crack tip stress state are investigated for parameters characterizing a PMMA/Al bimaterial. Additionally, the separate effects of elastic modulus mismatch and elastic wave speed mismatch on interface crack growth are explored for various PMMA-artificial material combinations. The mode mixity of the near tip fields is found to increase with increasing crack speed and in some cases large scale contact occurs in the vicinity of the crack tip. Crack speeds that exceed the smaller of the two Rayleigh wave speeds are also found.

1. Introduction

Fracture along or near an interface between phases plays a major role in limiting the toughness and ductility of multi-phase materials. This has motivated a substantial body of work on failure at interfaces. Nevertheless, a fracture mechanics framework for interfacial crack initiation and growth has been developed only relatively recently, see e.g., Rice [1], Shih [2], Hutchinson and Suo [3]. This late development is due, at least in part, to the fact that the identification of crack tip characterizing parameters for interfacial cracks is much less straightforward than for cracks in macroscopically homogeneous solids. For example, the elastic crack tip fields for a stationary interface crack in a body subject to pure mode I loading have both mode I and mode II components. Furthermore, because these fields are oscillatory, the mode mixity, the ratio of the mode I and mode II components, varies with distance from the crack tip. As a further complication, the near tip fields become compressive and give rise to contact across the bond line.

The extension of static fracture mechanics for homogeneous solids to interfacial fracture requires experiment to provide the toughness as a function of the mode mixity, with experimental studies showing that the apparent toughness increases as the ratio of mode II to mode I increases, as discussed, for example, in Hutchinson and Suo [3]. Since the mode mixity depends on distance from the crack tip, specification of the mixity also involves a characteristic length parameter. This is in contrast to the situation for homogeneous brittle solids where mode I crack initiation is characterized by a scalar parameter, e.g., a critical value of the stress intensity factor.

Interfacial fracture mechanics is even more complicated when crack growth and crack arrest under dynamic loading conditions are considered. For homogeneous brittle materials, the energy release rate as a function of crack speed (and possibly the amount of crack growth) is assumed to be a material property and known from experiment. Together with the singular elastic fields, which have an amplitude that depends on the loading, they give rise to a 'crack tip equation of motion,' Freund [4]. A similar approach for interfacial cracks would involve assuming that the energy release rate as a function of crack speed, of mode mixity and of the amount of crack growth is characteristic of a particular interface. Furthermore, the mode mixity varies with crack speed, Yang et al. [5], and the possible dependence on the crack speed of the characteristic length parameter used for specifying the mode mixity needs to be considered.

Theoretical studies of dynamic interfacial crack growth have been inhibited by the analytical complexity of the problem (even for crack growth along a bond line between two linear elastic materials) and by uncertainty concerning an appropriate fracture criterion. In spite of these difficulties basic problems of dynamic interfacial crack growth have been addressed by a number of authors, for example, Willis [6], Brock and Achenbach [7], Yang et al. [5], Liu et al. [8], Lo et al. [9]. In particular, Yang et al. [5] have obtained the singular fields for a crack growing dynamically along the bond line between two linear elastic materials. Their results, which pertain to crack speeds up to the Rayleigh wave speed of the more compliant of the two materials, give an oscillatory singularity, with the oscillation index becoming infinite at the smaller Rayleigh wave speed. Liu et al. [8] have presented crack tip singular fields for crack speeds greater than the smaller Rayleigh wave speed that are quite different from the sub-Rayleigh wave speed fields; for example, the order of the stress singularity depends on crack speed and is less than 1/2.

Recently, Rosakis and co-workers [8, 10, 11] have carried out a series of experimental studies of dynamic interfacial crack growth that give the crack speed history and the crack tip stress and strain fields under well-characterized conditions. The experimental results show crack speeds exceeding the smaller Rayleigh wave speed, increased mode mixity with increasing crack speed and the development of a contact region along the bond line. Several attempts have been made to develop interfacial fracture criteria that are consistent with the experimental results, [12, 13]. Lo et al. [9] have carried out finite element crack growth computations to simulate the experiments of Tippur and Rosakis [10]. They used a node release method in conjunction with a mode mixity and crack speed dependent critical energy release rate criterion. An iterative technique was used to obtain a criterion that gave a crack speed history consistent with the measurements. The extent to which such a criterion is characteristic of the interface and is independent of the specimen configuration and imposed loading history remains to be determined.

In this investigation, computations of dynamic interfacial crack growth are carried out where the crack speed history and the effect of inertia on the apparent toughness are direct outcomes of the analysis. The basis for the theoretical framework is the cohesive surface decohesion formulation in Needleman [14]. Crack initiation and crack growth are calculated directly in terms of the properties of the materials and of the parameters characterizing the cohesive surface separation law, which include a strength and the work of separation per unit area. Hence, a characteristic length enters the formulation. This framework has been used to address a variety of issues involving separation of surfaces in solids; in particular, quasi-static crack growth in homogeneous solids and along interfaces, Needleman [15, 16], Tvergaard and

Hutchinson [17, 18], and dynamic crack growth in homogeneous solids, Xu and Needleman [19, 20].

The specific problem analyzed is a planar bimaterial block with an initial central crack on the bond line. Plane strain conditions are assumed to prevail. Two types of loading are considered. In one case, a tensile load is applied to the material on one side of the bond line, while the opposite side of the specimen is fixed. In the other case, a separation is prescribed along a portion of the crack faces. Here, there is a single cohesive surface along the interface between the two solids so that the crack is constrained to grow along the bond line. In a subsequent study, Xu and Needleman [21], potential surfaces of decohesion are interspersed throughout the material as in Xu and Needleman [19, 20], and crack growth off the bond line is possible.

The focus in this investigation is on the evolution of the crack speed and of the crack tip stress and deformation fields for straight ahead crack growth. Calculations are carried out for a PMMA/Al bimaterial. In order to explore the effects of elastic mismatch and of different wave propagation characteristics, calculations are also carried out for PMMA bonded to several artificial materials, the properties of which are tailored to explore the effects of various bimaterial characteristics on interfacial crack propagation. Also, for comparison purposes, calculations are carried out for a homogeneous PMMA specimen, but with a cohesive surface along the bond line that is identical to the one used in the bimaterial analyses.

2. Problem formulation

The cohesive surface formulation and numerical method follow Xu and Needleman [19], where further details are given. A convected coordinate Lagrangian formulation is employed with the initial undeformed configuration taken as reference, so that all field quantities are considered to be functions of convected coordinates, y^i, which serve as particle labels, and time t. Relative to a fixed Cartesian frame, the position of a material point is denoted by $\mathbf{x}$ in the initial configuration and by $\bar{\mathbf{x}}$ in the current configuration. With the displacement vector and the deformation gradient defined as $\mathbf{u} = \bar{\mathbf{x}} - \mathbf{x}$ and $\mathbf{F} = \partial\bar{\mathbf{x}}/\partial\mathbf{x}$, respectively, the principle of virtual work is written in the form (Xu and Needleman [22])

$$\int_V \mathbf{s}\colon \delta\mathbf{F}\, \mathrm{d}V - \int_{S_{\mathrm{int}}} \mathbf{T}\cdot\delta\boldsymbol{\Delta}\, \mathrm{d}S = \int_{S_{\mathrm{ext}}} \mathbf{T}\cdot\delta\mathbf{u}\, \mathrm{d}S - \int_V \rho\frac{\partial^2\mathbf{u}}{\partial t^2}\cdot\delta\mathbf{u}\, \mathrm{d}V, \tag{1}$$

where $\mathbf{s}$ is the nonsymmetric nominal stress tensor, ρ is the density of the material in the reference configuration, $\boldsymbol{\Delta}$ is the displacement jump across the cohesive surface and $\mathbf{T} = \boldsymbol{\nu}\cdot\mathbf{s}$ is the traction vector on a surface with normal $\boldsymbol{\nu}$ in the reference configuration. Also, V, S_{ext} and S_{int} are the volume, external surface area and internal cohesive surface area, respectively.

Computations are carried out for center cracked bimaterial specimens, with initial height $2L$ and initial width $2w$, as sketched in Fig. 1(a). Plane strain conditions are assumed to prevail and a Cartesian coordinate system is used as reference, with the $y^1 - y^2$ plane as the plane of deformation. The specimen consists of two materials bonded along $y^2 = 0$ with a crack of initial length $2a_i$ along the bond line. At $t = 0$, the body is stress free and at rest, so that $\mathbf{u}(y^1, y^2, 0) = 0$ and $\dot{\mathbf{u}}(y^1, y^2, 0) = 0$. Attention is restricted to deformations that remain symmetric about $y^1 = 0$, with the region analyzed numerically being $y^1 \geqslant 0$.

Two types of loading are applied to the specimen. For both types of loading, symmetry about the y^2-axis requires

$$u^1 = 0, \quad T^2 = 0 \quad \text{on } y^1 = 0 \tag{2}$$

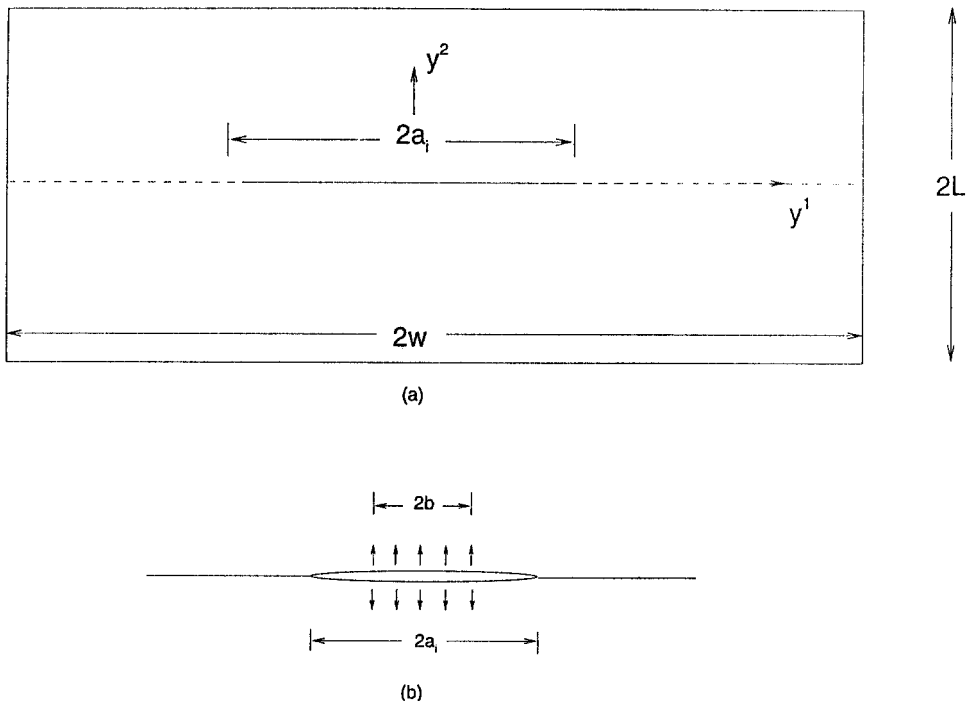

Fig. 1. (a) Geometry of the center cracked specimen. (b) Sketch illustrating the crack face loading.

and the lateral sides remain traction free, so that

$$T^1 = 0, \quad T^2 = 0 \quad \text{on} \quad y^1 = w. \tag{3}$$

In one case, tensile loading is applied to the boundary of the specimen along $y^2 = L$ and the opposite boundary ($y^2 = -L$) is fixed in the y^2-direction. The boundary conditions on $y^2 = \pm L$ are,

$$u_2 = \int V(t)\,\mathrm{d}t, \quad T^1 = 0 \quad \text{on} \quad y^2 = L, \tag{4}$$

$$u_2 = 0, \quad T^1 = 0 \quad \text{on} \quad y^2 = -L, \tag{5}$$

$$T^1 = T^2 = 0 \quad \text{on} \quad y^2 = 0 \quad \text{and} \quad 0 \leqslant y^1 \leqslant a_i. \tag{6}$$

In the other case, the loading is applied on the crack surfaces. The loading width is $2b$ so that $T^1 = T^2 = 0$ on $y^2 = 0$ and $b < y^1 < a_i$. The loading is applied symmetrically about $y^1 = 0$ as indicated in Fig. 1(b), with

$$u_2 = \int V(t)\,\mathrm{d}t, \quad T^1 = 0 \quad \text{on} \quad y^2 = 0^+ \quad \text{and} \quad 0 \leqslant y^1 \leqslant b, \tag{7}$$

$$u_2 = \int -V(t)\,\mathrm{d}t, \quad T^1 = 0 \quad \text{on} \quad y^2 = 0^- \quad \text{and} \quad 0 \leqslant y^1 \leqslant b, \tag{8}$$

and with stress free boundaries so that in addition to (3),

$$T^1 = 0, \quad T^2 = 0 \quad \text{on} \quad y^2 = \pm L. \tag{9}$$

Although the loading (7) and (8) on the crack faces is symmetrical, the crack tip is not loaded symmetrically because of the different wave speeds and elastic moduli of the bimaterial constituents.

In (4), (7) and (8), $V(t)$ is taken as

$$V(t) = \begin{cases} V_1 t/t_r, & \text{for } t \leqslant t_r; \\ V_1, & \text{for } t > t_r \end{cases}, \tag{10}$$

with V_1 being a prescribed velocity and the rise time, t_r, fixed at 0.1 μs, which is short enough to simulate impact loading, while being long enough to avoid numerical difficulties associated with step loading. The two loading cases are referred to subsequently as the 'boundary loading' and 'crack face loading' cases, respectively.

As in previous work, e.g. [14], [19], the continuum is characterized by two constitutive relations; a volumetric constitutive law that relates stress and strain, and a cohesive surface constitutive relation between the tractions and displacement jumps across one or more cohesive surfaces. Attention is confined to a single cohesive surface along the line $y^2 = 0$ in front of the initial crack, so that the crack is constrained to grow along the bond line.

The volumetric constitutive law for each material is taken to be that for an isotropic hyperelastic solid so that

$$\mathbf{S} = \frac{\partial W}{\partial \mathbf{E}} \qquad W = \tfrac{1}{2}\mathbf{E}\colon \mathbf{L}\colon \mathbf{E}. \tag{11}$$

Here W is the strain energy density and $\mathbf{L}$ is the tensor of isotropic elastic moduli with two elastic constants, Young's modulus E and Poisson's ratio ν. The second Piola–Kirchhoff stress, $\mathbf{S}$, and the Lagrangian strain, $\mathbf{E}$, are given by

$$\mathbf{S} = \mathbf{s} \cdot \mathbf{F}^{-T} \quad \mathbf{E} = \tfrac{1}{2}(\mathbf{F}^T \cdot \mathbf{F} - \mathbf{I}) \tag{12}$$

where $\mathbf{I}$ is the identity tensor, $(\ )^{-1}$ denotes the inverse, and $(\ )^T$ denotes the transpose.

The constitutive law for a cohesive surface relates the traction and displacement jump across the surface and is taken to be elastic so that any dissipation associated with separation is neglected. The traction across the surface is given by

$$\mathbf{T} = -\frac{\partial \phi}{\partial \boldsymbol{\Delta}}. \tag{13}$$

Because the cohesive surface constitutive relation is one between the traction and displacement jump across the surface, a characteristic length is introduced. The behavior depends on the ratio of the specimen size to this characteristic length. The specimen dimensions in the calculations here are of the order of $10^3 - 10^4$ times the cohesive surface characteristic length. In this regime, the response with a crack-like defect depends mainly on the cohesive surface strength and work of separation, and is not sensitive to details of the potential shape, [15, 16].

In two dimensions, the specific form used for the potential ϕ is one given in Xu and Needleman [23] that allows for tangential, as well as normal, decohesion

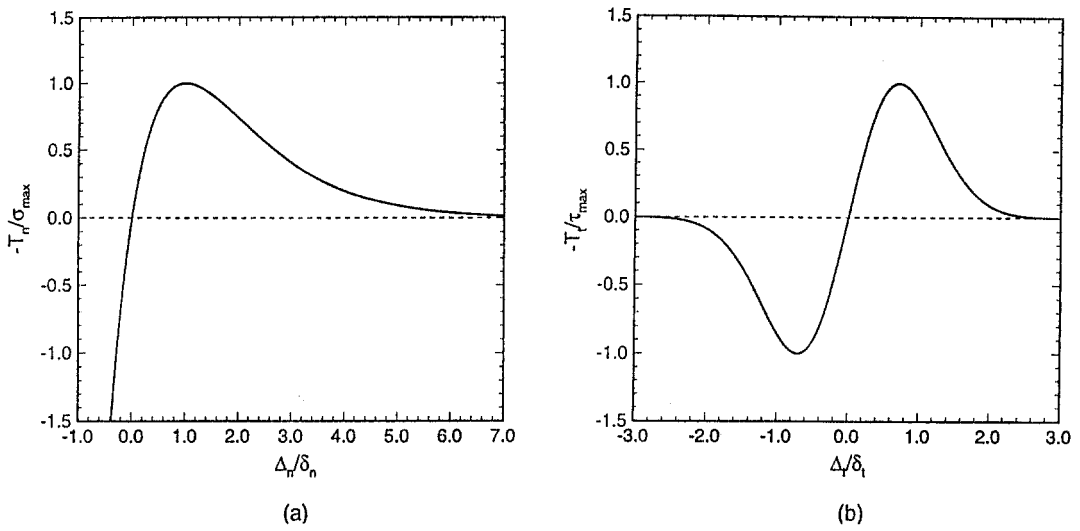

Fig. 2. (a) Normal traction, T_n, across the cohesive surface as a function of Δ_n with $\Delta_t \equiv 0$. (b) Shear traction, T_t, across the cohesive surface as a function of Δ_t for $\Delta_n \equiv 0$.

$$\phi(\boldsymbol{\Delta}) = \phi_n + \phi_n \exp\left(-\frac{\Delta_n}{\delta_n}\right) \times \left\{\left[1 - r + \frac{\Delta_n}{\delta_n}\right]\frac{1-q}{r-1} - \left[q + \left(\frac{r-q}{r-1}\right)\frac{\Delta_n}{\delta_n}\right]\exp\left(-\frac{\Delta_t^2}{\delta_t^2}\right)\right\}, \tag{14}$$

where $\Delta_n = \mathbf{n} \cdot \boldsymbol{\Delta}$ and $\Delta_t = \mathbf{t} \cdot \boldsymbol{\Delta}$, with $\mathbf{n}$ and $\mathbf{t}$ as the normal and tangent, respectively, to the surface at a given point in the reference configuration. Also, $q = \phi_t/\phi_n$ and $r = \Delta_n^*/\delta_n$, where Δ_n^* is the value of Δ_n after complete shear separation with normal traction $T_n = 0$. The normal work of separation, ϕ_n, and the shear work of separation, ϕ_t, can be written as

$$\phi_n = e\sigma_{\max}\delta_n \qquad \phi_t = \sqrt{\frac{e}{2}}\tau_{\max}\delta_t. \tag{15}$$

Here, $e = \exp(1)$, and $\sigma_{\max}$ and $\tau_{\max}$ are the cohesive surface normal strength and tangential strength, respectively, and δ_n and δ_t are corresponding characteristic lengths.

Figure 2(a) shows the normal traction across the surface, T_n, as a function of Δ_n with $\Delta_t \equiv 0$. The maximum value of $-T_n$ is $\sigma_{\max}$ and occurs when $\Delta_n = \delta_n$. The variation of shear traction T_t with Δ_t when $\Delta_n \equiv 0$, is shown in Fig. 2(b). The maximum value of $|T_t| = \tau_{\max}$ is attained when $|\Delta_t| = \sqrt{2}\delta_t/2$.

Although a full finite deformation formulation is used, the overall response is accurately described by linear isotropic elasticity, except locally where new free surface is being created. Key parameters are the elastic wave speeds and the elastic mismatch parameters introduced by Dundurs [24]. For each material, the speeds of dilatational, shear and Rayleigh surface waves are (see, e.g., Freund [4])

$$c_d = \sqrt{\frac{E(1-\nu)}{\rho(1+\nu)(1-2\nu)}}, \qquad c_s = \sqrt{\frac{E}{2\rho(1+\nu)}},$$

$$c_R = c_s \frac{0.862 + 1.14\nu}{1 + \nu}. \tag{16}$$

For static plane problems of bimaterials, Dundurs [24] observed that isotropic elastic solutions depend on only two non-dimensional combinations of the elastic moduli. Dundurs' [24] elastic mismatch parameters are defined as

$$\alpha = \frac{E_a(1-\nu_b^2) - E_b(1-\nu_a^2)}{E_a(1-\nu_b^2) + E_b(1-\nu_a^2)},$$
$$\beta = \frac{1}{2}\frac{E_a(1-2\nu_b)(1+\nu_b) - E_b(1-2\nu_a)(1+\nu_a)}{E_a(1-\nu_b^2) + E_b(1-\nu_a^2)}, \tag{17}$$

where the subscripts a and b refer to the two materials.

For a stationary interface crack, the singular near-tip fields give rise to tractions on $y^2 = 0$ directly ahead of the crack tip that have the form (England [25], Erdogan [26], Rice and Sih [27], Rice [1]),

$$T^2 + iT^1 = \frac{(K_1 + iK_2)}{\sqrt{2\pi y^1}}(y^1)^{i\varepsilon} \qquad i = \sqrt{-1}, \tag{18}$$

where K_1 and K_2 are, respectively, the mode I and mode II stress intensity factors and the oscillatory index ε is defined by

$$\varepsilon = \frac{1}{2\pi} \ln \frac{1-\beta}{1+\beta}. \tag{19}$$

The static interfacial crack tip fields differ from those for homogeneous materials in several significant respects, [1–3]. First, near-tip interface crack tip fields are mixed mode, involving both tension (mode I) and shear (mode II), for purely tensile remote loading. The ratio of shear to normal traction ahead of the crack tip varies with distance from the tip due to the oscillatory nature of the singularity. Furthermore, the normal traction on the bond line becomes compressive implying that contact occurs in the vicinity of the crack tip. The extent of the contact region and how close it is to the crack tip depends on the value of ε and on the remote loading. For values of ε characteristic of actual bimaterial systems and for tensile loading of the sort considered here, contact for a stationary crack occurs extremely close to the crack tip; at distances where the idealization of a mathematically sharp crack in a linear elastic medium is questionable (see, for example [3]). For a dynamically running interface crack, the value of ε depends on the crack speed as well as on the elastic constants and, as the crack speed approaches the smaller of the two Rayleigh wave speeds, $\varepsilon \to \infty$, Yang et al. [5]. The implications of this are that at high crack speeds (but at speeds less than the smaller Rayleigh wave speed) the strength of the mode II component increases with crack speed, and that contact occurs over a larger region and further from the crack tip than for the corresponding stationary crack.

The generalization of Rice's [28] J-integral for dynamic loading conditions can be expressed as, Nakamura et al. [29],

$$J = \int_\Gamma [(W + K)\,\mathrm{d}y^2 - T^i u_{i,1}\,\mathrm{d}s] + \int_A \left[\rho \frac{\partial^2 u^i}{\partial t^2} u_{i,1} - \rho \frac{\partial u^i}{\partial t}\left(\frac{\partial u_i}{\partial t}\right)_{,1}\right] \mathrm{d}A, \tag{20}$$

where W is the strain energy density given in (11), K is the kinetic energy

$$K = \tfrac{1}{2}\rho \frac{\partial u^i}{\partial t}\frac{\partial u_i}{\partial t}, \tag{21}$$

Γ is a path in the reference configuration surrounding the crack tip (for the case where crack face loading Γ intersects the crack face in $b < y^1 < a_i$) and A is the area inside the contour Γ. For an interface crack constrained to grow parallel to the y^1-axis, the value of J in (20) is independent of the particular path Γ surrounding the crack tip. Also, for an ideal crack, J is the energy release rate in the limit $\Gamma \to 0$ when certain conditions are met, Nakamura et al. [29], which involve, at least, the crack speed being less than the smaller Rayleigh wave speed.

The finite element discretization is based on linear displacement triangular elements that are arranged in a 'crossed-triangle' quadrilateral pattern. When the finite element discretization of the displacement field is substituted into the principle of virtual work (1) and the integrations are carried out, the discretized equations of motion are obtained as

$$\mathbf{M}\frac{\partial^2 \mathbf{U}}{\partial t^2} = \mathbf{R}, \tag{22}$$

where $\mathbf{U}$ is the vector of nodal displacements, $\mathbf{M}$ is the mass matrix and $\mathbf{R}$ is the nodal force vector consisting of contributions from the area elements and the cohesive surfaces. A lumped mass matrix is used in (22) instead of the consistent mass matrix, since this has been found preferable for explicit time integration procedures, from the point of view of accuracy as well as computational efficiency, Krieg and Key [30]. An explicit time integration scheme that is based on the Newmark β-method is used to integrate (22) to obtain the nodal velocities and the nodal displacements (Belytschko et al. [31]). Further description of the numerical procedure can be found in [19].

Initially, there is a well-defined crack tip location. Once crack growth initiates, this is no longer the case because of the continuous dependence of the cohesive surface tractions on the displacement jump $\boldsymbol{\Delta}$. For presentation of the results, the largest value of y^1 for which $\Delta_n \geqslant 5\delta_n$ is recorded together with the current time. This value of y^1 is denoted by a and is identified with the current crack tip position. A quadratic polynomial is fitted through three points of the a versus t curve, say a_{n-1}, a_n and a_{n+1}, and the slope of this quadratic at t_n is taken as the crack speed at $t_n, \dot{a}_n$. In [19], it was shown that the predictions of crack location and crack speed were not sensitive to the choice of using other values of Δ_n to define the crack location.

3. Numerical results

The geometry of the specimen is specified by $L = 2.8$ mm, $w = 3.05$ mm, $a_i = 0.25$ mm and, for the crack face loading cases, $b = 0.2$ mm (see Fig. 1). The specimen dimensions are taken to be small for numerical convenience, but are large enough, compared with the cohesive surface characteristic length, for crack-like response to be obtained. The main effect of the small specimen size is the relatively short time interval before wave reflections from the specimen surfaces reach the crack tip.

The finite element mesh consists of 23,300 quadrilateral elements and 94,920 degrees of freedom, with a uniform region around the interface ahead of the initial crack surrounded by

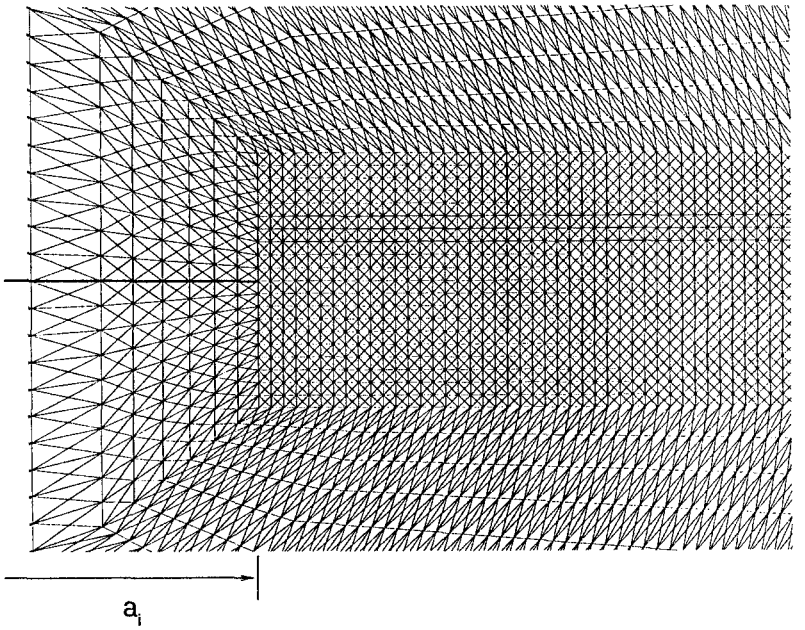

Fig. 3. Finite element mesh near the initial crack tip. Each quadrilateral consists of four 'crossed' triangles. The uniform mesh region extends for 400 quadrilaterals in front of the initial crack tip, but an extent of only 43 quadrilaterals is shown. In the computations here, a_i is always taken to be 0.25 mm.

a graduated mesh out to the specimen boundaries. The uniform region has 400 × 20 square elements, with side length 0.004 mm (see Fig. 3).

The parameters characterizing the cohesive surface along the bond line are: $\sigma_{\max} = 162.0$ MPa $(E_{\text{PMMA}}/20)$, $\tau_{\max} = 377.7$ MPa and $\delta_n = \delta_t = 4.0 \times 10^{-7}$ m, so that $q = 1$ with $\phi_n = \phi_t = 176.2$ J/m^2. The remaining cohesive parameter r is taken to be zero. The magnitude of $\sigma_{\max}$ is half that used to characterize homogeneous PMMA in [19], and the value of the work of separation is close to the value of the energy release rate at crack initiation (150 J/m^2) measured by Tippur and Rosakis [10] for a PMMA/Al bimaterial. The side length of the quadrilaterals in Fig. 3 is 1.6 times that of the finest of the meshes in [19], where the same value of δ_n was used.

Experimental results, e.g., Liechti and Chai [32], show a strong dependence of interfacial toughness on mode mixity (the ratio of shear to tension near the crack tip). However, this does not necessarily mean that the intrinsic toughness of the cohesive surface depends on the mode mixity. It may very well be that this effect arises because of the change in near tip fields. For example, as suggested by Liechti and Chai [32], increased shear can tend to facilitate inelastic deformation. In any case, in the present calculations, there is no intrinsic dependence of the interface toughness on the mode of separation.

3.1. Dynamic cracking along a PMMA/Al interface

The material parameters and elastic wave speeds for PMMA and aluminum are given in Table 1. Dundurs' parameters (17) and the oscillatory index ε in (19) for the PMMA/Al combination are listed in Table 2.

Figure 4(a) shows curves of crack speed, $\dot{a}$, versus time for boundary loading on the PMMA side with $V_1 = 15$ m/s. (The very high frequency oscillations in the crack speed versus time

Table 1. Material properties

Material	E(GPa)	ν	ρ(kg/m^3)	c_d(m/s)	c_s(m/s)	c_R(m/s)
PMMA	3.24	0.35	1190	2090	1004	938
Al	80.0	0.3	2700	6316	3376	3127
Material A	6.44	0.15	5950	1069	686	616
Material B	6.44	0.15	2380	1690	1085	974
Material C	80.0	0.35	29380	2090	1004	938

Table 2. Dundurs' parameters and oscillatory indices

Bimaterial combination	α	β	ε (static)
PMMA/Al	−0.9194	−0.21	0.06784
PMMA/material A	−0.2817	0.0	0.0
PMMA/material B	−0.2817	0.0	0.0
PMMA/material C	−0.9222	−0.2128	0.06879

curves are a consequence of the numerics.) Crack growth starts soon after the arrival of the loading wave at $t = 1.34$ μs. Because of the impedance mismatch across the bond line, some of the wave is reflected and some is transmitted. The transmitted wave is reflected back by the fixed boundary at $y^2 = -L$ and arrives at the interface at $t = 2.23$ μs which causes an increase in crack speed. The crack speed exceeds the Rayleigh wave speed of PMMA and then decreases a little when the compressive reflected wave arrives at $t = 3.11$ μs. For comparison purposes, crack speed versus time curves for a homogeneous PMMA specimen, with the same bond line cohesive properties, are shown in Fig. 4(a) for impact velocities of $V_1 = 30$ m/s and $V_1 = 15$ m/s. Since both halves of the specimen are PMMA, there are no wave reflections along the bond line. Crack growth starts soon after the arrival of the loading wave at $t = 1.34$ μs and the crack speed rapidly reaches a constant. With $V_1 = 30$ m/s, this constant is the Rayleigh wave speed while with $V_1 = 15$ m/s, the limiting crack speed is 89 percent of the Rayleigh wave speed. For a given impact velocity, the interface crack reaches a higher speed than does a corresponding crack in a homogeneous solid. Also, the crack acceleration, the time interval over which the more or less steady crack speed is reached, is smaller for the interface crack than for the homogeneous solid.

Curves of the J-integral (20) versus time are shown in Fig. 4(b) for the three cases in Fig. 4(a). Crack growth begins when J has increased to ϕ_n (as it should, Rice [28]). The path integral J was computed on several contours ignoring any contribution of the cohesive surface; sufficiently far away from the current crack tip path independent J values were obtained. For homogeneous PMMA, J is nearly constant during the early stages of crack growth; with $V_1 = 15$ m/s, J slowly exceeds ϕ_n, while with $V_1 = 30$ m/s, J increases more rapidly. For the crack along the PMMA/Al bimaterial interface, growth also initiates when $J \approx \phi_n$, J is then nearly constant for some time interval and then oscillates. The mean value of J increases as the crack speed increases.

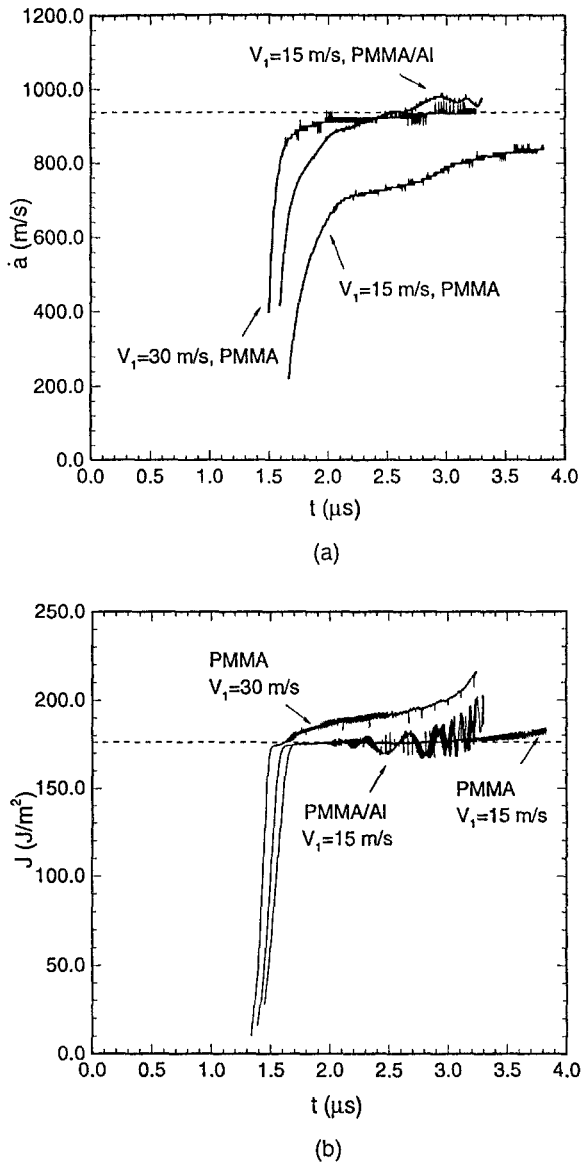

Fig. 4. Crack speed, $\dot{a}$, versus time, t, (a) and J-integral versus time (b) for an interface crack between PMMA and aluminum with boundary loading velocity $V_1 = 15$ m/s. For comparison purposes results are also shown for homogeneous PMMA with $V_1 = 30$ m/s and $V_1 = 15$ m/s. In (a) the dashed line indicates the Rayleigh wave speed of PMMA and in (b) the dashed line corresponds to $J = \phi_n$.

Since the crack is subject to tensile loading, the mode of crack growth in homogeneous PMMA is mode I. On the other hand, for the PMMA/Al interface crack, the mode of crack opening involves both mode I and mode II components, with an increasing mode II contribution as the crack speed increases. This is seen in Fig. 5, which shows the normal, Δ_n, and tangential, Δ_t, displacement jumps across the bond line near the current crack tip at four stages of crack growth. Note that the steep slope of the curves of Δ_n/δ_n versus y^1 near the crack tip in Fig. 5 indicate that the crack tip location is not too sensitive to the value of Δ_n/δ_n used to identify it. In the latter three stages, Figs. 5(b), 5(c) and 5(d), the crack speed exceeds the PMMA

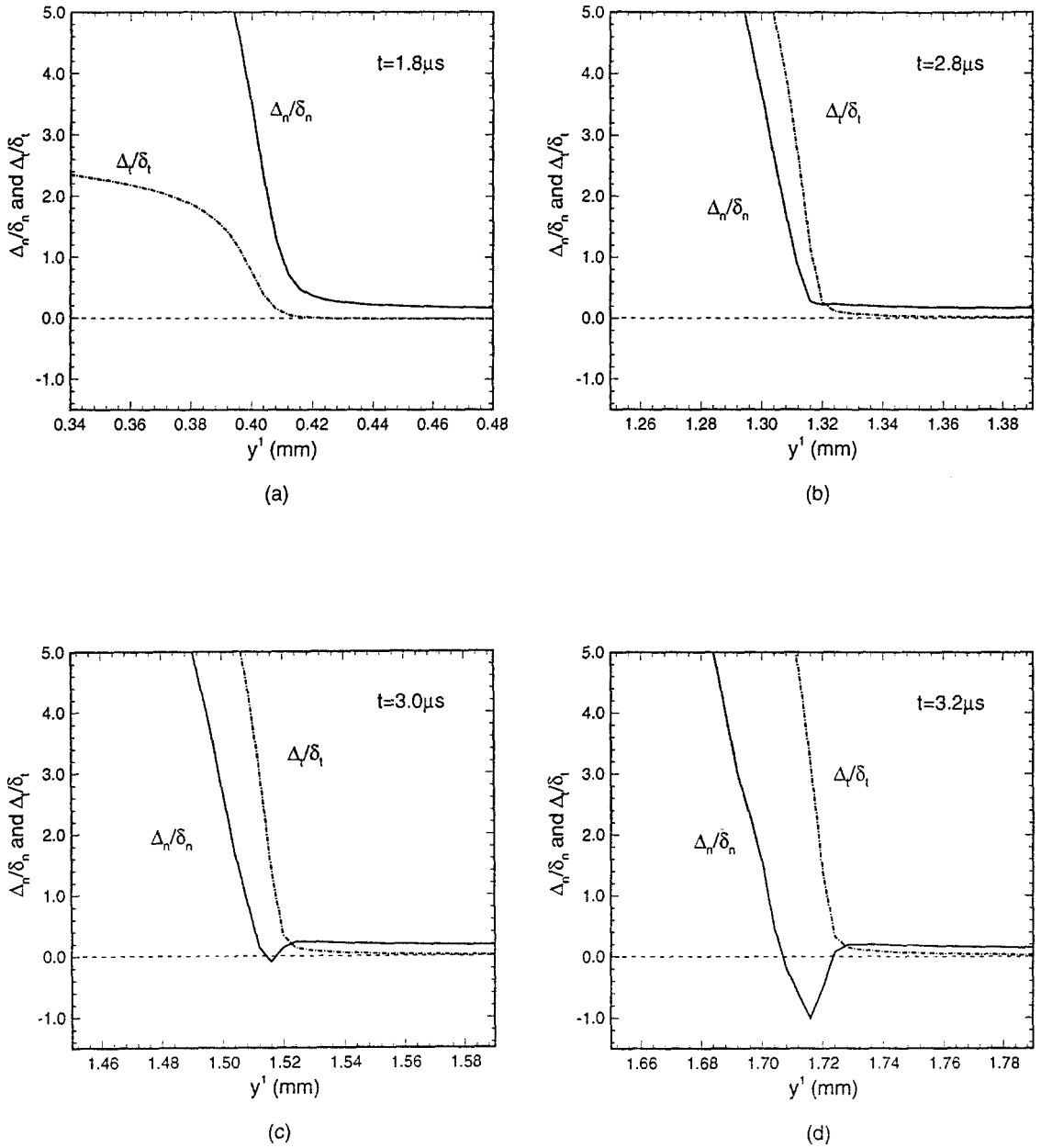

Fig. 5. Normal and tangential components of the displacement jump across the bond line near the current crack tip for an interface crack between PMMA and aluminum with boundary loading velocity $V_1 = 15$ m/s. (a) At $t = 1.8$ μs, $a = 0.394$ mm and $\dot{a} = 784$ m/s. (b) At $t = 2.8$ μs, $a = 1.295$ mm and $\dot{a} = 961$ m/s. (c) At $t = 3.0$ μs, $a = 1.491$ mm and $\dot{a} = 974$ m/s. (d) At $t = 3.2$ μs, $a = 1.684$ mm and $\dot{a} = 970$ m/s.

Rayleigh wave speed. At $t = 1.8$ μs, Fig. 5(a), the crack opening mode is clearly mode I dominated. The relative magnitude of the tangential component increases and at $t \approx 2.3$ μs, the normal and tangential opening components are about equal ahead of the crack. Figure 5(b) shows the situation at $t = 2.8$ μs, where Δ_t/δ_t exceeds Δ_n/δ_n (recall that in the calculations here $\delta_n = \delta_t$). At $t = 3.0$ μs($a = 1.491$ mm), a contact zone develops in front of the crack tip and at the last stage shown, the extent of the contact zone (where $\Delta_n < 0$) is about 18 μm,

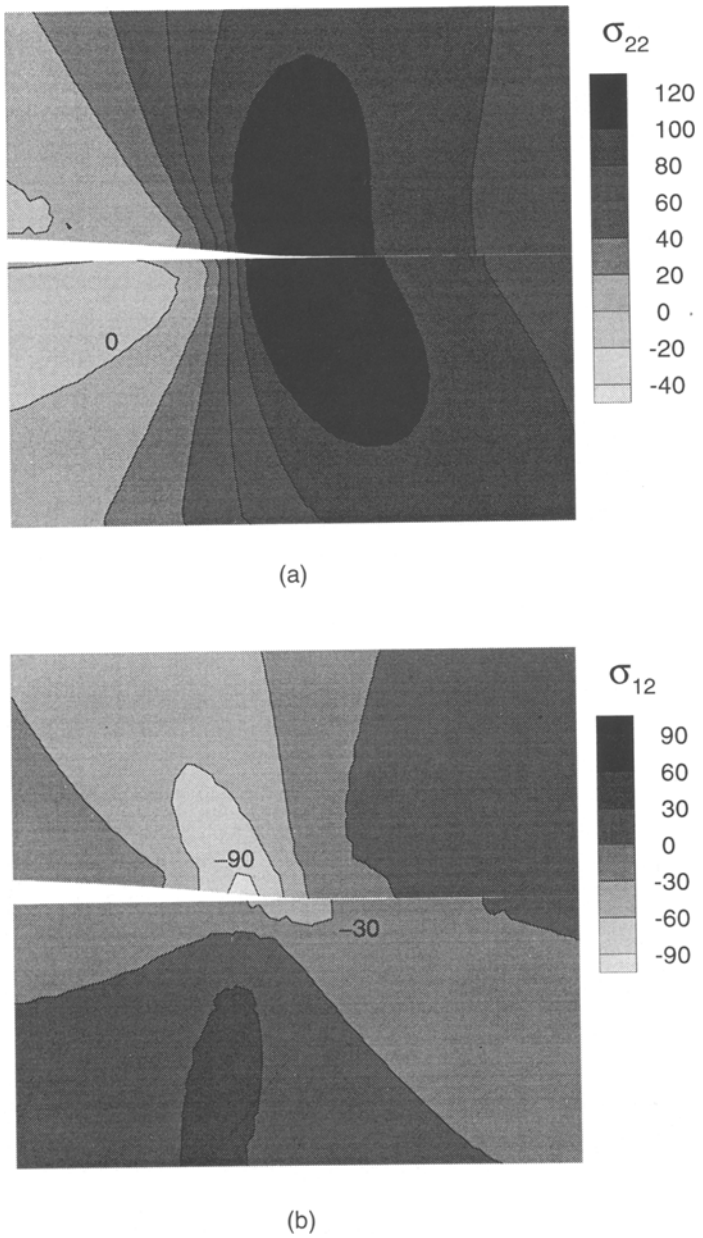

Fig. 6. Contours of physical components of Cauchy stress at $t = 1.8\ \mu$s($a = 0.394$ mm and $\dot{a} = 784$ m/s) for an interface crack between PMMA and aluminum with boundary loading velocity $V_1 = 15$ m/s. The upper half of the specimen is PMMA and the lower half is aluminum. The extent of the region shown is 0.083 mm in the y^1-direction and 0.076 mm in the y^2-direction. (a) Axial component σ_{22}. (b) Shear component σ_{12}.

which is 45 δ_n. The maximum compressive displacement in the contact zone in Fig. 5(d) is about δ_n. In Fig. 4(b), the oscillation in the value of J begins at $\approx 2.4\ \mu$s, which in Fig. 5 corresponds to a shift from a mode I to a mode II dominant opening mode. Also, the frequency of the oscillations in J increases at about 3.0 μs, with the initiation of bond line contact.

The change in crack opening mode is reflected in the surrounding field. Figures 6(a) and 6(b) show contours of the physical axial component of Cauchy stress, σ_{22}, and of the physical shear component of Cauchy stress, σ_{12}, at $t = 1.8$ μs, respectively. At this time, the crack speed is 84 percent of the Rayleigh wave speed of PMMA. Although the mixed mode nature of the stress field is evident in Fig. 6, the near-tip stress state is mainly tensile.

Contours of the physical axial component of Cauchy stress, σ_{22}, at four times are shown in Fig. 7, while contours of the physical shear component of Cauchy stress, σ_{12}, at the same times are shown in Fig. 8. The four times in Figs. 7 and 8 are $t = 2.0$, 2.8, 3.0 and 3.2 μs, with corresponding crack speeds of 93 percent, 102 percent, 104 percent and 103 percent of the Rayleigh wave speed of PMMA. Comparing Fig. 6 with Figs. 7(a) and 8(a) shows the effect of increasing crack speed below the smaller of the two Rayleigh wave speeds of the bimaterial, while the remaining plots in Figs. 7 and 8 show stress distributions for crack speeds that exceed the smaller Rayleigh wave speed.

With increasing crack speed, the region of high axial stress contracts on the PMMA side and the region of high shear stress expands. When the crack speed is less than the PMMA Rayleigh wave speed, the highest values of σ_{22} occur near the crack tip (Figs. 6(a) and 7(a)). However, when the crack speed is greater than the PMMA Rayleigh wave speed the largest values of σ_{22} occur well off the bond line. As a result of the compressive traction that occurs because of contact, a region of negative σ_{22} develops in front of the apparent crack tip. In Fig. 8, the distance between the location of the maximum magnitude of the shear stress and the location of the apparent crack tip along the bond line increases as the contact zone grows.

The dynamics of crack growth are quite different for the case of crack face loading. Figure 9(a) compares curves of crack speed, $\dot{a}$, versus time for a PMMA/Al bimaterial specimen and for a homogeneous PMMA specimen. In both cases, the impact velocity is $V_1 = 30$ m/s. Crack growth starts somewhat after the arrival of the PMMA Rayleigh surface wave at $t = 0.053$ μs. As in the case of boundary loading, the crack speed for the bimaterial is significantly greater than for the corresponding homogeneous solid. For the PMMA/Al bimaterial in Fig. 9(a), the crack speed eventually exceeds in Rayleigh wave speed of PMMA. For homogeneous PMMA, the crack speed at the termination of the calculation in Fig. 9(a) is about 64 percent of the Rayleigh wave speed of PMMA.

The evolution of the dynamic J-integral (20) in Fig. 9(b) is also different for crack face loading than for boundary loading. Of course, crack initiation still occurs when $J = \phi_n$, Rice [28]. For homogeneous PMMA, J decreases slightly. A similar decreasing trend is seen for the PMMA/Al bimaterial, until $t = 1.60$ μs, at which point J begins to increase and undergo high frequency oscillations. This coincides with the crack speed exceeding the PMMA Rayleigh wave speed.

Figures 10(a) and 10(b) show the normal and tangential displacement jumps across the bond line at $t = 1.6$ μs and at $t = 2.0$ μs for the PMMA/Al bimaterial with crack face loading. At $t = 1.6$ μs, $a = 1.344$ mm and $\dot{a} = 935$ m/s, the crack opening mode is mode I dominated, while at $t = 2.0$ μs, $a = 1.727$ mm and $\dot{a} = 983$ m/s, which is 4.8 percent above the PMMA Rayleigh wave speed, the normal and tangential components are about equal ahead of the current crack tip. With crack face loading, no contact zone develops over the range of the calculation. Corresponding contour plots of axial and shear stress at $t = 2.0$ μs are shown in Fig. 11(a) and 11(b). The largest value of the axial stress component σ_{22} in PMMA occurs well away from the bond line.

The calculations are terminated when the crack nears the end of the constant mesh region. Thus, the development of a contact zone may eventually take place for the PMMA/Al specimen

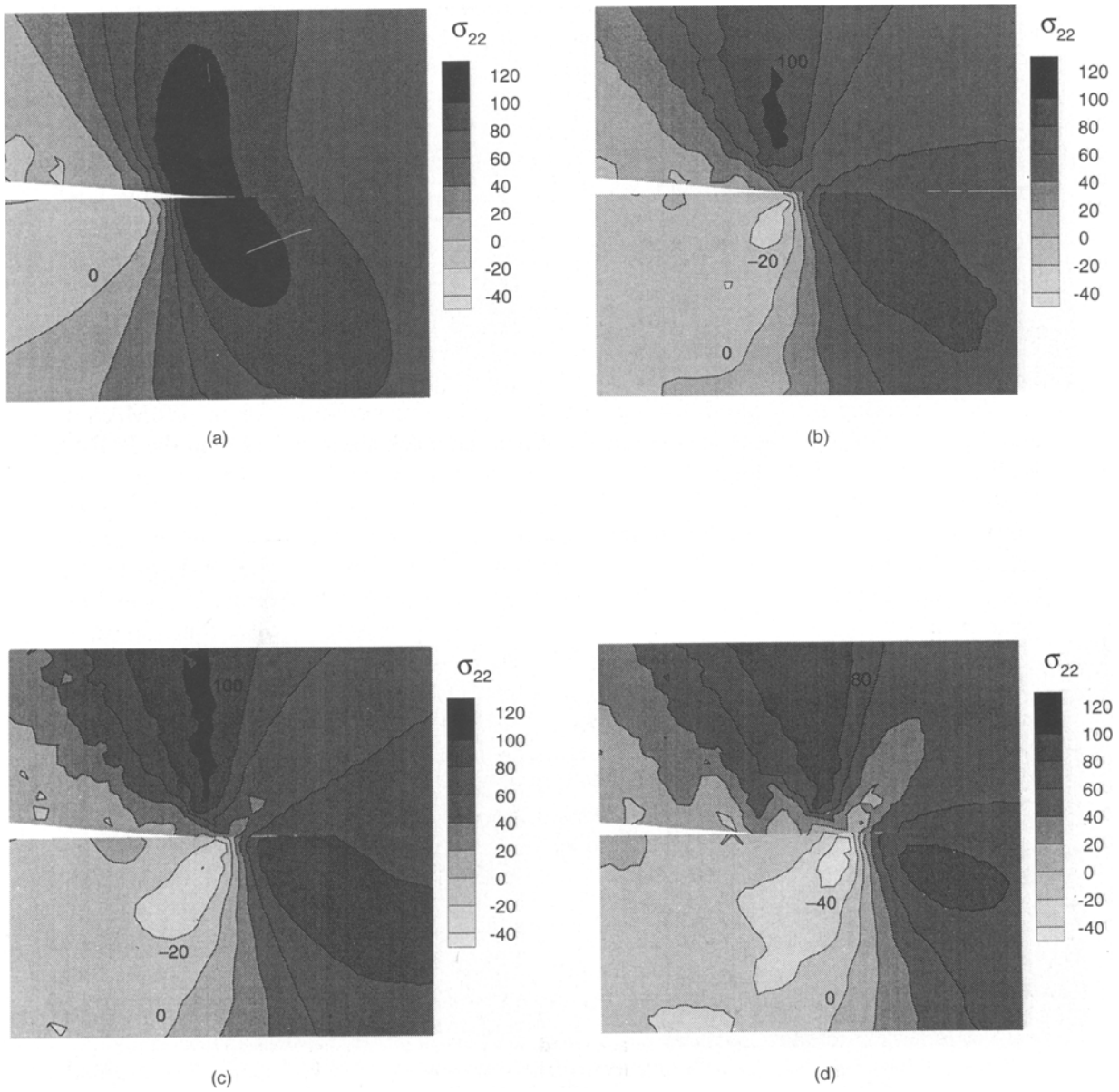

Fig. 7. Contours of the physical axial component of Cauchy stress, σ_{22}, for an interface crack between PMMA and aluminum with boundary loading velocity $V_1 = 15$ m/s. The upper half of the specimen is PMMA and the lower half is aluminum. The extent of the region shown is 0.083 mm in the y^1-direction and 0.076 mm in the y^2-direction. (a) At $t = 2.0$ μs, $a = 0.562$ mm and $\dot{a} = 871$ m/s. (b) At $t = 2.8$ μs, $a = 1.295$ mm and $\dot{a} = 961$ m/s. (c) At $t = 3.0$ μs, $a = 1.491$ mm and $\dot{a} = 974$ m/s. (d) At $t = 3.2$ μs, $a = 1.684$ mm and $\dot{a} = 970$ m/s.

with crack face loading. However, the calculations here indicate that it would at least require more crack growth to develop a contact zone for this type of loading than for tensile boundary loading.

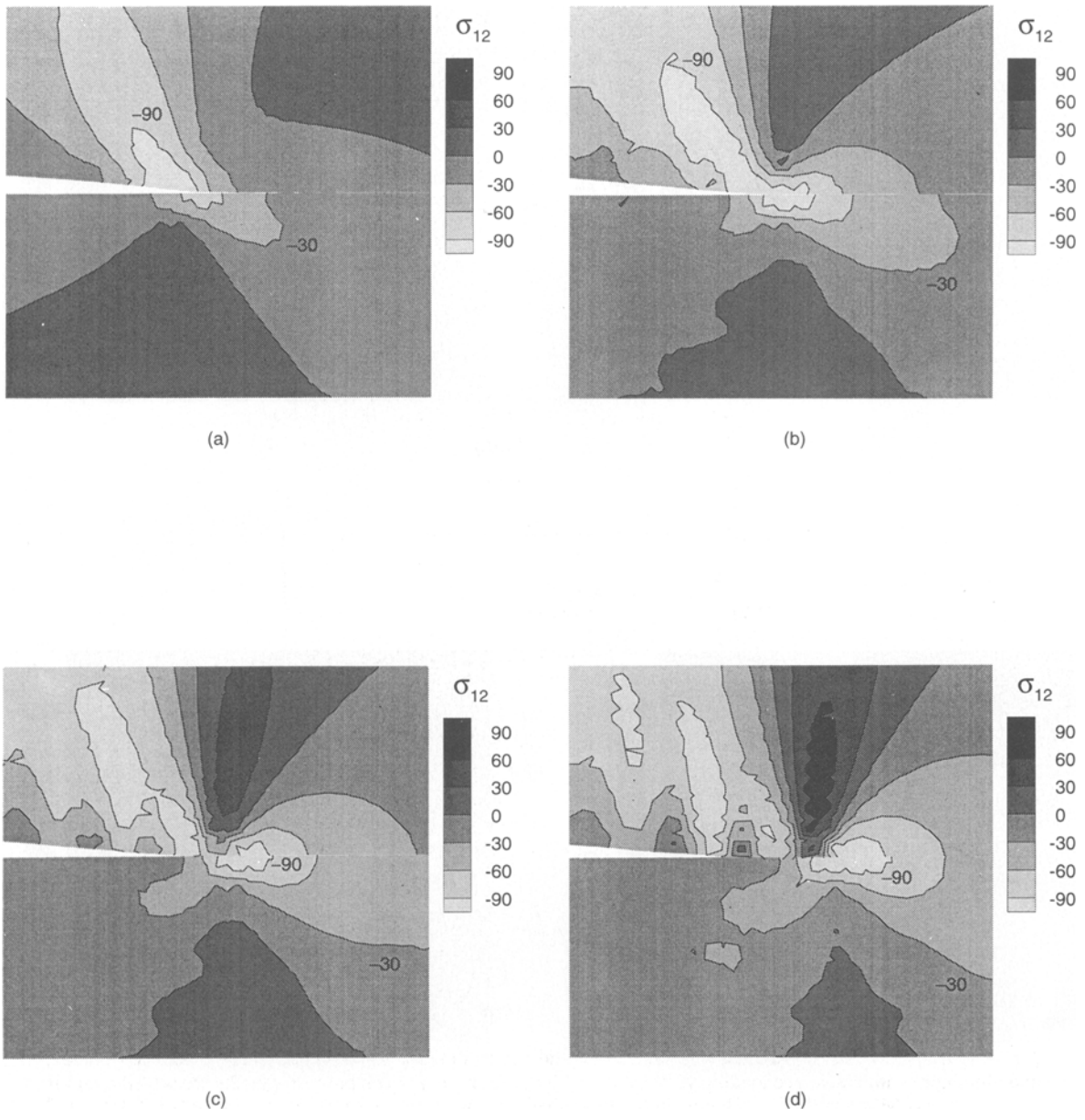

Fig. 8. Contours of the physical shear component of Cauchy stress, σ_{12}, for an interface crack between PMMA and aluminum with boundary loading velocity $V_I = 15$ m/s. The upper half of the specimen is PMMA and the lower half is aluminum. The extent of the region shown is 0.083 mm in the y^1-direction and 0.076 mm in the y^2-direction. (a) At $t = 2.0$ μs, $a = 0.562$ mm and $\dot{a} = 871$ m/s. (b) At $t = 2.8$ μs, $a = 1.295$ mm and $\dot{a} = 961$ m/s. (c) At $t = 3.0$ μs, $a = 1.491$ mm and $\dot{a} = 974$ m/s. (d) At $t = 3.2$ μs, $a = 1.684$ mm and $\dot{a} = 970$ m/s.

3.2. Parameter study

In order to explore the role of stiffness and wave speed mismatch across the bond line on the crack growth response, calculations are carried out for various PMMA bimaterial

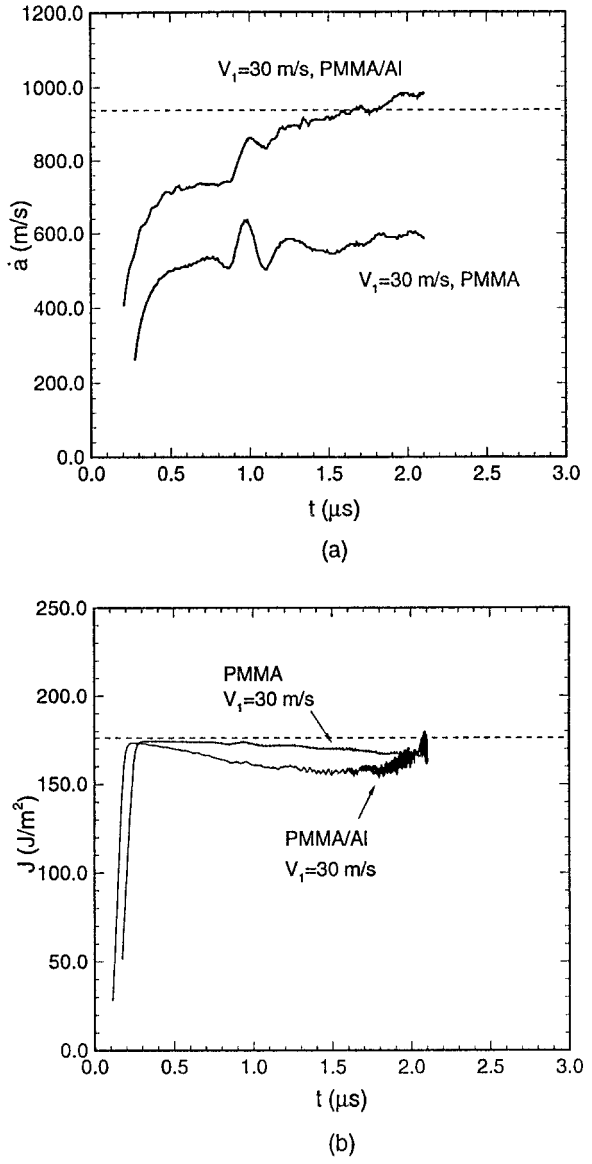

Fig. 9. Crack speed, $\dot{a}$, versus time, t, (a) and J-integral versus time (b) for an interface crack between PMMA and aluminum with crack face loading velocity $V_1 = 30$ m/s. For comparison purposes results are also shown for homogeneous PMMA with $V_1 = 30$ m/s. In (a) the dashed line indicates the Rayleigh wave speed of PMMA and in (b) the dashed line corresponds to $J = \phi_n$.

combinations. The elastic constants and density of the artificial materials in Table 1 are chosen to obtain certain mismatch characteristics. The combination of properties so chosen are termed material A, material B and material C, with the corresponding PMMA bimaterial characteristics given in Table 2. Subsequently, for the case of boundary loading, the material on the loading side will be listed first; for example, PMMA/MA will be used to refer to the PMMA – material A bimaterial with loading on the PMMA side and MA/PMMA to refer to the PMMA – material A bimaterial with loading on the material A side. The material on the

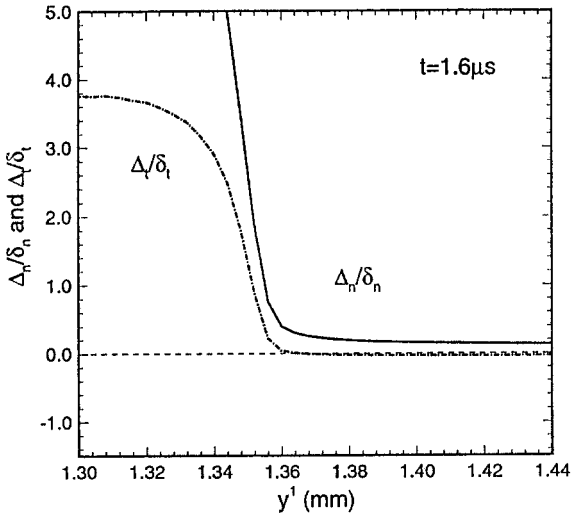

(a)

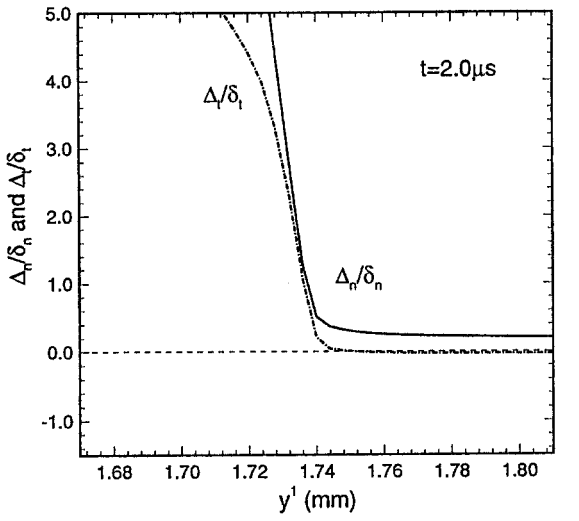

(b)

Fig. 10. Normal and tangential components of the displacement jump across the bond line near the current crack tip for an interface crack between PMMA and aluminum with crack face loading velocity $V_1 = 30$ m/s. (a) At $t = 1.6$ μs, $a = 1.344$ mm and $\dot{a} = 935$ m/s. (b) At $t = 2.0$ μs, $a = 1.727$ mm and $\dot{a} = 983$ m/s.

loading side occupies the part of the specimen where $y^2 > 0$. With crack face loading, PMMA is taken to occupy the region $y^2 > 0$.

Material A has elastic properties for which the Dundurs' parameter β in (17) and therefore the oscillatory index ε in (19) is zero. Material A also has elastic wave speeds that are smaller than those of PMMA. The parameters β and ε are also zero for material B, but with the elastic wave speed mismatch much smaller than for the PMMA/MA combination. Additionally, both the shear wave speed, c_s, and the Rayleigh wave speed, c_R, for material B are greater than for PMMA. The Dundurs' parameters for the PMMA/MC combination are essentially the

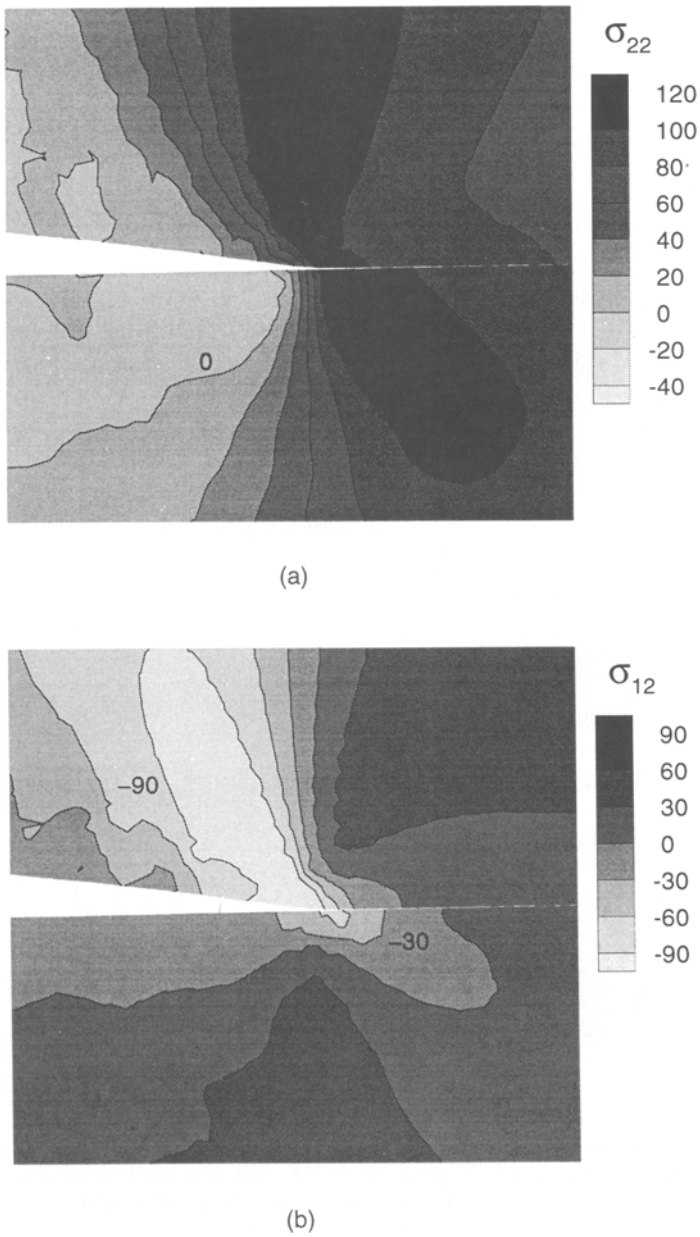

Fig. 11. Contours of physical components of Cauchy stress at $t = 2.0$ μs($a = 1.727$ mm and $\dot{a} = 983$ m/s) for an interface crack between PMMA and aluminum with crack face loading velocity $V_1 = 30$ m/s. The upper half of the specimen is PMMA and the lower half is aluminum. The extent of the region shown is 0.083 mm in the y^1-direction and 0.076 mm in the y^2-direction. (a) Axial component σ_{22}. (b) Shear component σ_{12}.

same as for PMMA/Al, but with the elastic wave speeds of material C and PMMA being the same.

Another possibly relevant wave speed is the Stonely wave speed. Stonely waves are interfacial waves and whether or not they can occur depends on the material property mismatch across the interface, see e.g. Achenbach [33]. The PMMA/MC bimaterial is the only one of

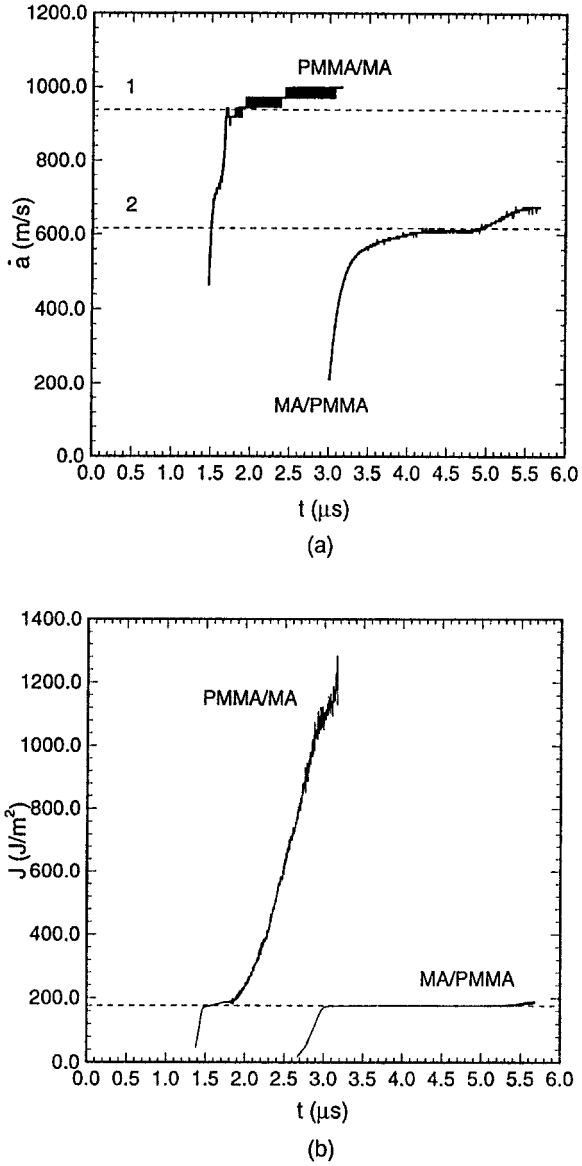

Fig. 12. Crack speed, $\dot{a}$, versus time, t, (a) and J-integral versus time (b) for interface cracks with $\varepsilon = 0$ (PMMA/MA and MA/PMMA). The loading velocity for PMMA/MA (boundary loading on the PMMA side) is $V_1 = 30$ m/s and is $V_1 = 11.73$ m/s for MA/PMMA (boundary loading on the material A side). In both cases, the stress carried by the wave is 74.6 MPa. In (a) the dashed lines indicate the Rayleigh wave speed of PMMA (1) material A (2), and in (b) the dashed line corresponds to $J = \phi_n$.

the four bimaterial combinations considered for which there is a real Stonely wave speed, which is 948 m/s.

Figure 12 shows crack speed, $\dot{a}$, and J-integral versus time curves for PMMA/MA and MA/PMMA bimaterials subject to remote tensile loading. For PMMA/MA, where impact tensile loading is applied on the PMMA side, $V_1 = 30$ m/s, while for MA/PMMA, the loading is applied on the material A side with $V_1 = 11.73$ m/s. In both cases, the stress carried by the wave is 74.6 MPa. With the loading applied on the PMMA side, the crack starts to grow after the wave reaches the initial crack tip at $t = 1.34$ μs. The crack speed increases very

rapidly and reaches a plateau of 985 m/s, which exceeds the Rayleigh wave speed of PMMA by 5 percent. Perhaps more significantly, the crack speed is 160 percent of the Rayleigh wave speed of material A and is even close to (92 percent of) the dilatational wave speed of material A. When the loading is on the material A side, crack growth begins after the arrival of the loading wave at $t = 2.62$ μs, the crack accelerates and then grows at a rather constant speed that is the Rayleigh wave speed of MA (616 m/s). The transmitted wave is reflected back by the fixed boundary at $y^2 = -L$ and arrives at the bond line at $t = 5.29$ μs. The crack speed then increases to 670 m/s.

In Fig. 12(b), for both PMMA/MA and MA/PMMA, crack growth begins when J has increased to ϕ_n and the value of J is relatively constant while the crack speed increases. For PMMA/MA, J increase sharply at around 1.9 μs, which is when the crack speed reaches the Rayleigh wave speed of PMMA (which is the larger Rayleigh wave speed for the PMMA/MA bimaterial). At the end of the calculation, it is seven times ϕ_n. On the other hand, for loading on the material A side (MA/PMMA), J remains relatively constant at ϕ_n and only increases slowly when the crack speed exceeds the Rayleigh wave speed of material A.

The partitioning of kinetic and strain energy between PMMA and material A is shown in Fig. 13. In Fig. 13(a), which is for the case of boundary loading on the PMMA side, the strain energy and the kinetic energy in PMMA increase monotonically until $t = 1.34$ μs, which is when the wave arrives at the bond line. Since material A is stiffer, the reflected wave is tensile and the strain energy of the PMMA side continues to increase while the kinetic energy of the PMMA side decreases slightly. At $t = 2.68$ μs, the reflected wave reaches $y^2 = L$, after which both the strain energy and the kinetic energy in PMMA increase. Due to the transmitted tensile wave, the strain energy and kinetic energy in material A increase monotonically. In Fig. 13(b), as the loading is on the side of the stiffer material (material A), the initial tensile wave is reflected back as a compressive wave at $t = 2.62$ μs. The strain energy in material A decreases but the kinetic energy increases until the reflected compressive wave reaches $y^2 = L$ at $t = 5.24$ μs. The transmitted tensile wave is reflected by the fixed boundary ($y^2 = -L$) at $t = 3.96$ μs after which the strain energy in PMMA increases while the kinetic energy in PMMA decreases. Since the material constitutive relations and the cohesive surface constitutive relation are elastic, no energy dissipation mechanisms are incorporated into the formulation. Although not shown here, it should be noted that the energy balance was checked, namely that the work done by the imposed loading was equal to the sum of the material strain and kinetic energies and the elastic energy stored in the cohesive surfaces.

The contour plots in Fig. 14 show that when loading is applied on the PMMA side, the crack tip fields have a strong shear (mode II) component in the latter stages of crack growth. The largest values of the opening stress σ_{22} occur off the bond line. However, the largest shear stress magnitudes (negative values of σ_{12}) do occur near the current crack tip. The asymptotic crack tip field of Liu et al. [13] for an elastic solid bonded to a rigid substrate, with the crack speed greater than the shear wave speed of the elastic solid, has a singular line emanating from the crack tip across which infinite stress and velocity jumps occur. The orientation of this singular line is a function of the ratio of the crack speed to the shear wave speed of the elastic solid. Identifying material A with the elastic solid in the analysis of Liu et al. [13] because the elastic wave speeds of material A are much less than those of PMMA, even though Young's modulus for material A is greater than that for PMMA (see Table 1), gives a crack speed to shear wave velocity ratio of 1.44. This corresponds to the singular line being $\approx 135°$ from the bond line, which is in good agreement with the location of the concentration in Fig. 14(a). The oscillating contours in Fig. 14 also suggest 'stress wave trapping' near the crack tip due

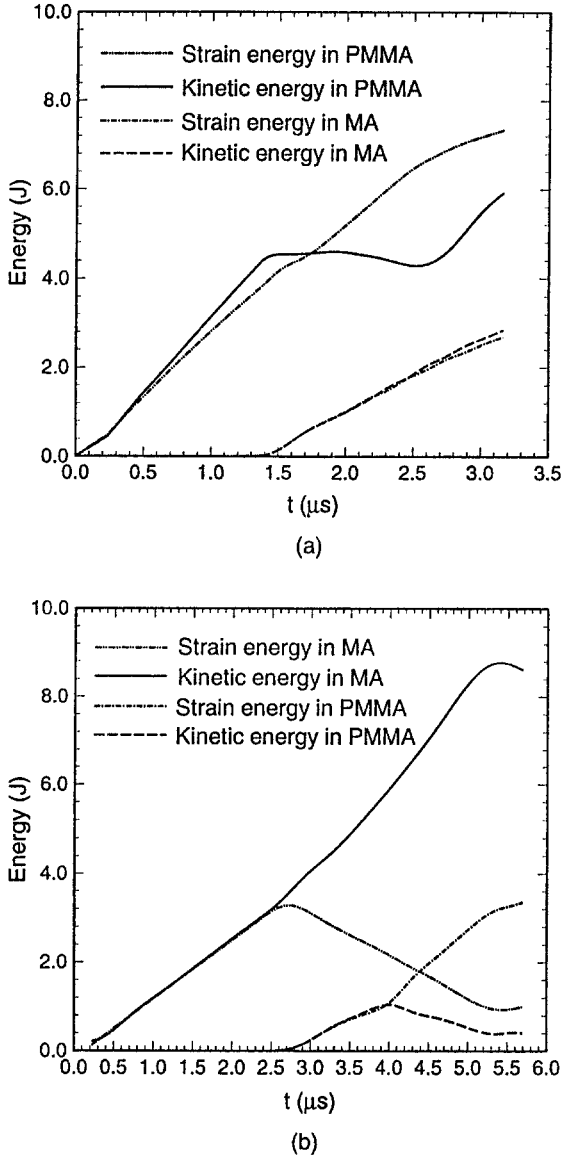

Fig. 13. Energy variations in PMMA and material A as a function of time for PMMA/MA and MA/PMMA (the energy is calculated for a unit thickness, 1 m, out of the plane of deformation). (a) For PMMA/MA (boundary loading on the PMMA side). (b) For MA/PMMA (boundary loading on the material A side).

to the relatively slow wave speeds of material A. On the other hand, for MA/PMMA where the loading is applied on the material A side, Fig. 15, the crack speed is much slower and the peak value of σ_{22} is near the crack tip. Note that the near tip shear stress is positive in Fig. 15. Figure 16 shows that the opening mode is shear dominated for PMMA/MA but tensile dominated for MA/PMMA. In addition, contact occurs for the PMMA/MA case while no contact occurs for the MA/PMMA case.

A calculation was also carried out for the PMMA/MA bimaterial with crack face loading. Curves of crack speed, $\dot{a}$, versus time and of the J-integral versus time, with $V_1 = 30$ m/s, are shown in Figs. 17(a) and 17(b), respectively. For comparison purposes, results of a calculation

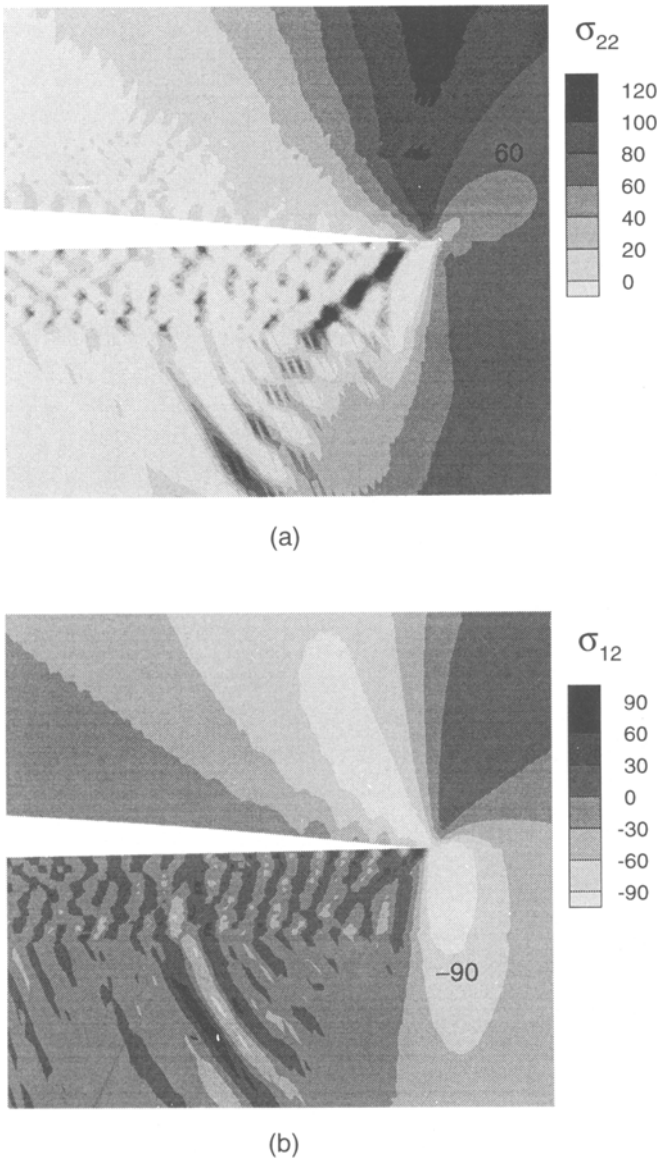

Fig. 14. Contours of physical components of Cauchy stress at $t = 3.0$ μs ($a = 1.674$ mm and $\dot{a} = 985$ m/s) for PMMA/MA (boundary loading on the PMMA side) with $V_1 = 30$ m/s. The upper half of the specimen is PMMA and the lower half is material A. The extent of the region shown is 0.25 mm in the y^1-direction and 0.23 mm in the y^2-direction. (a) Axial component σ_{22}. (b) Shear component σ_{12}.

for homogeneous PMMA and $V_1 = 30$ m/s are also shown. The crack speed curve for the bimaterial is about 15 percent below that for homogeneous PMMA, but the J versus time curve is about the same. The crack speeds remain less than either of the Rayleigh wave speeds and, in contrast to the boundary loading calculations, the value of J decreases with time. The crack tip opening mode is mode I dominant over the range of the calculation and contact does not occur.

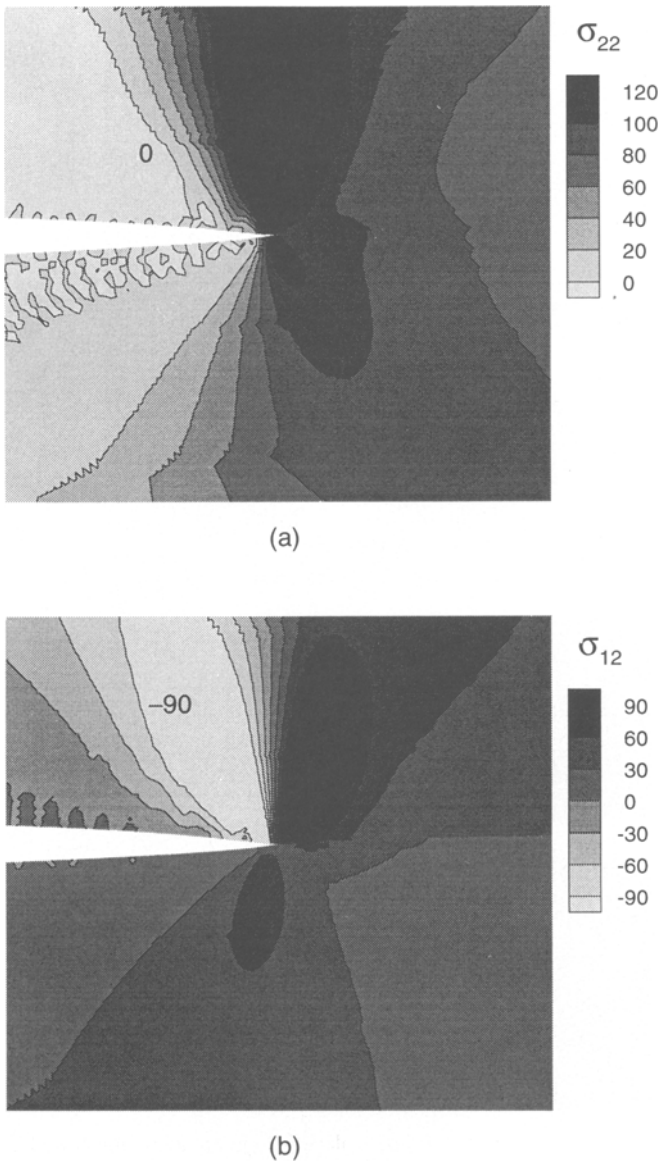

Fig. 15. Contours of physical components of Cauchy stress at $t = 5.68\ \mu$s ($a = 1.838$ mm and $\dot{a} = 670$ m/s) for MA/PMMA (boundary loading on the MA side) with $V_1 = 11.73$ m/s. The upper half of the specimen is material A and the lower half is PMMA. The extent of the region shown is 0.25 mm in the y^1-direction and 0.23 mm in the y^2-direction. (a) Axial component σ_{22}. (b) Shear component σ_{12}.

Figures 18(a) and 18(b), respectively, show curves of crack speed, $\dot{a}$, versus time and J-integral versus time for PMMA/MB, with boundary loading on PMMA side. The elastic constants of materials A and B are the same, but the density of material B is 40 percent that of material A. From the densities and elastic wave speeds, the amplitude of the reflected wave from PMMA/MB is about 50 percent of the reflected wave for PMMA/MA (e.g., Achenbach [33, p. 187]). The crack speed reaches a value of 976 m/s, very similar to that for the corresponding PMMA/MA calculation, but the value of J increases rather slowly to a

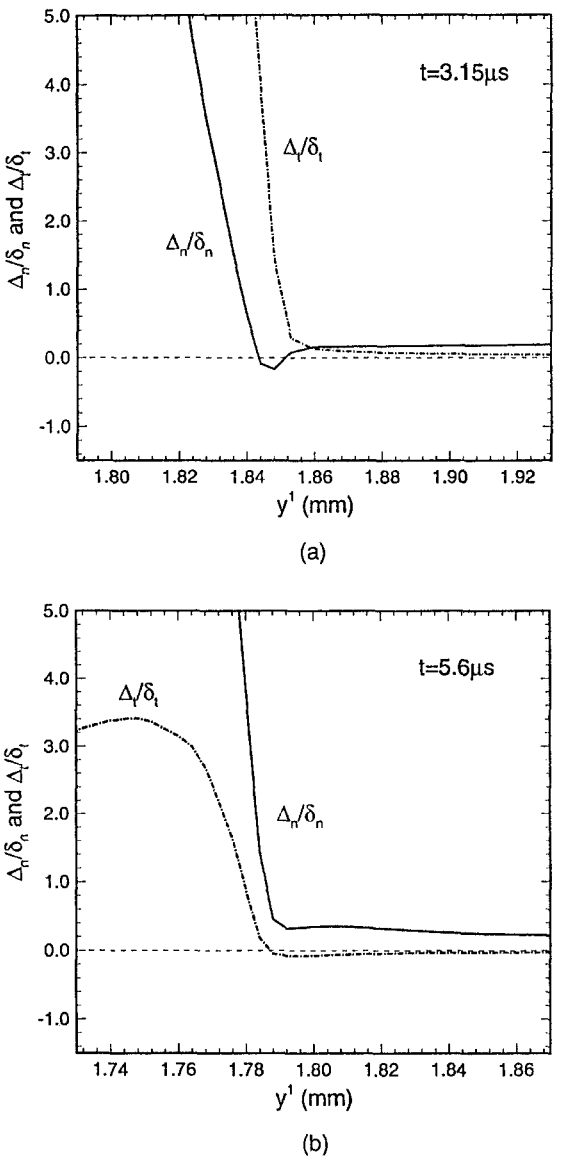

Fig. 16. Normal and tangential components of the displacement jump across the bond line near the current crack tip. (a) For PMMA/MA (boundary loading on the PMMA side) at $t = 3.15$ μs, $a = 1.824$ mm and $\dot{a} = 985$ m/s. (b) For MA/PMMA (boundary loading on the material A side) at $t = 5.6$ μs, $a = 1.778$ mm and $\dot{a} = 670$ m/s.

value which is only slightly larger than ϕ_n. The contour plots in Fig. 19 show that the region of high values of the axial stress component σ_{22} is much larger on the material B side than on the PMMA side. Even though the crack speed is very similar to that for PMMA/MA, the crack tip fields in Fig. 19 differ substantially from those in Fig. 14. Figure 20(a) shows that the opening mode is mainly tensile, although the shear displacement jump is substantial, and that contact does not occur.

Results for a PMMA/MC bimaterial, with boundary loading magnitude $V_1 = 15$ m/s applied on the PMMA side are shown in Fig. 21. In Fig. 21(a), the crack speed increases and reaches the Rayleigh wave speed, similar to the case of homogeneous PMMA with

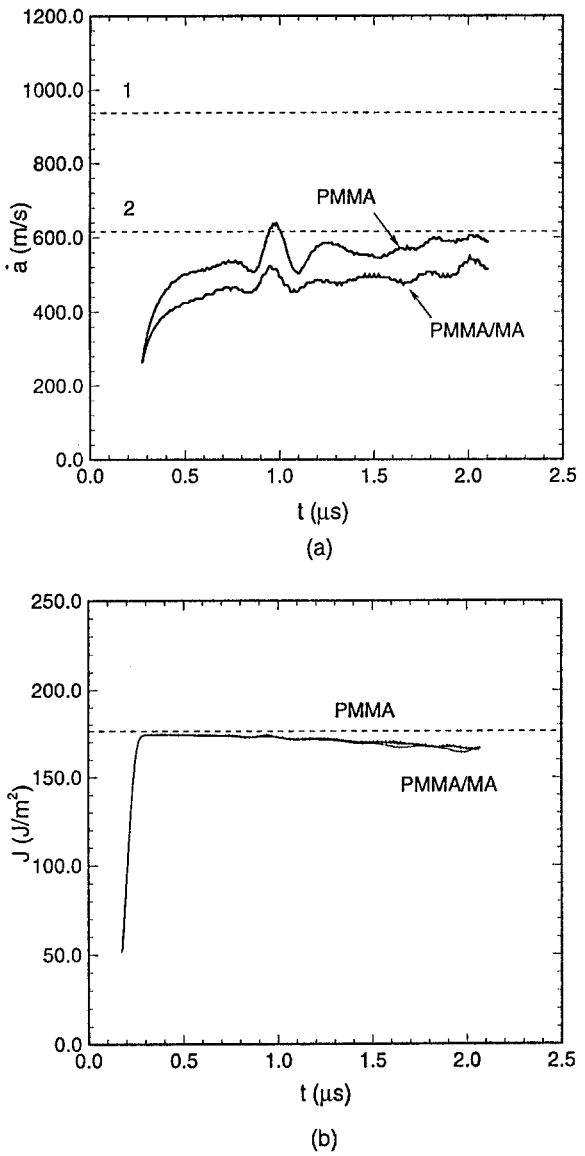

Fig. 17. Crack speed, $\dot{a}$, versus time, t, (a) and J-integral versus time (b) for an interface crack in PMMA/MA with crack face loading velocity $V_1 = 30$ m/s. For comparison purposes results are also shown for homogeneous PMMA with $V_1 = 30$ m/s. In (a) the dashed lines indicate the Rayleigh wave speed of PMMA (1) and material A (2), and in (b) the dashed line corresponds to $J = \phi_n$.

$V_1 = 30$ m/s. This may be due to the stress level after the wave reflection from the bond line at $y^2 = 0$ in the PMMA/MC specimen being about the same as that in homogeneous PMMA with $V_1 = 30$ m/s. The value of J in Fig. 21(b) is nearly constant at ϕ_n as the crack speed increases and J increases when the crack speed becomes constant. For PMMA/MC, the crack opening mode changes from being tensile dominated in the early stages of crack growth to being shear dominated in the later stages of crack growth. On the other hand, the crack opening mode remains tensile for homogeneous PMMA. For PMMA/MC, the oscillation in J starts at 2.2 μs, which is when the crack tip opening mode becomes shear dominated. The value

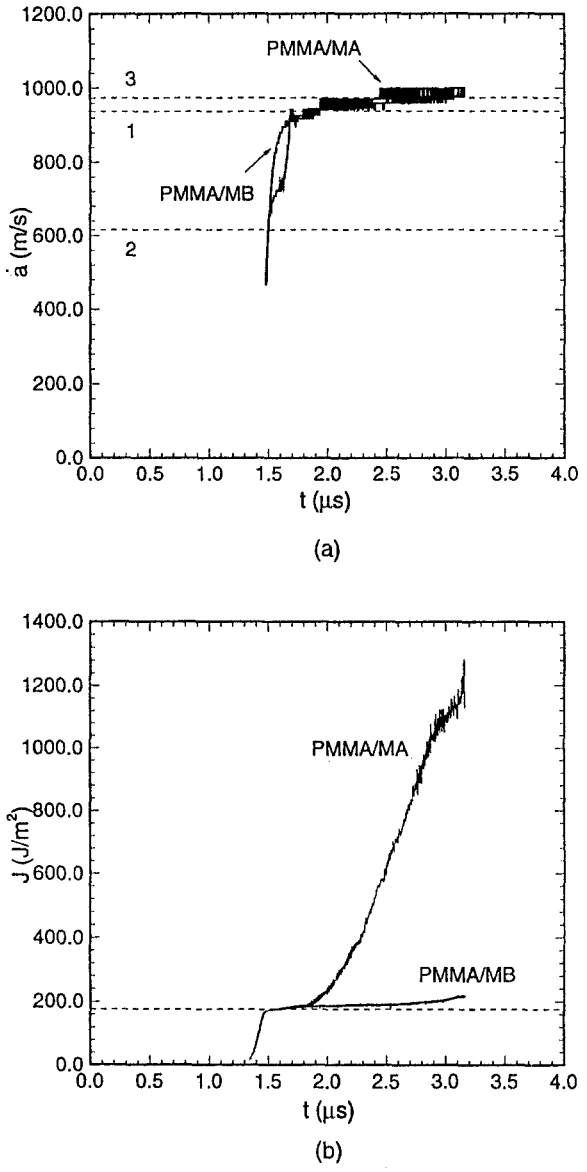

Fig. 18. Crack speed, $\dot{a}$, versus time, t, (a) and J-integral versus time (b) for an interface crack in PMMA/MB (boundary loading on the PMMA side) with $V_1 = 30$ m/s. For comparison purposes results are also shown for PMMA/MA with $V_1 = 30$ m/s. In (a) the dashed lines indicate the Rayleigh wave speed of PMMA (1), material A (2), and material B (3), and in (b) the dashed line corresponds to $J = \phi_n$.

of J increases sharply at 3.0 μs, which is when the crack speed reaches the Rayleigh wave speed (both materials have the same wave speeds). A plot of the opening mode at $t = 3.2$ μs is shown in Fig. 20(b). Similar plots at various times between 2.0 μs and 3.2 μs (not shown here) indicate that contact has not occurred in this case.

Figure 22 shows corresponding curves of crack speed, $\dot{a}$, versus time and of the J-integral versus time for PMMA/MC with crack face loading having $V_1 = 30$ m/s. In Fig. 22(a), the crack speed curve for the PMMA/MC bimaterial is about 15 percent above that for homogeneous PMMA. The J versus time curve for the PMMA/MC bimaterial in Fig. 22(b)

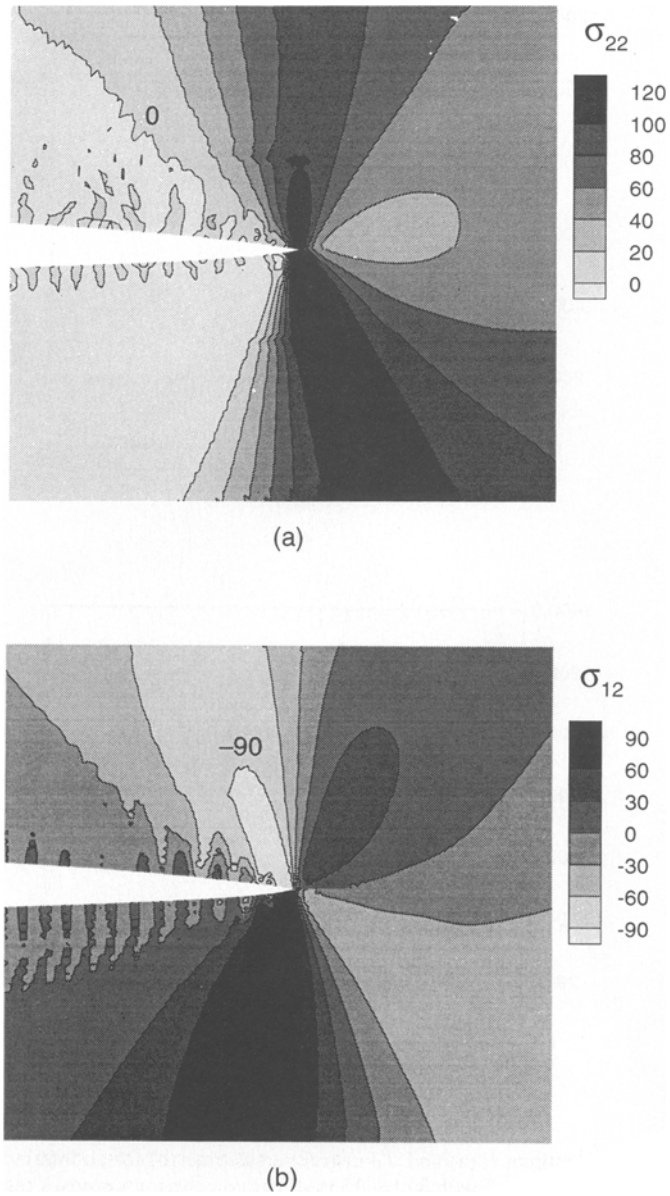

Fig. 19. Contours of physical components of Cauchy stress at $t = 3.0$ μs ($a = 1.678$ mm and $\dot{a} = 976$ m/s) for PMMA/MB (boundary loading on the PMMA side) with $V_1 = 30$ m/s. The upper half of the specimen is PMMA and the lower half is material B. The extent of the region shown is 0.25 mm in the y^1direction and 0.23 mm in the y^2-direction. (a) Axial component σ_{22}. (b) Shear component σ_{12}.

decreases rapidly while that for homogeneous PMMA only decreases slightly. The contour plots in Fig. 23, although differing in detail, having a qualitative similarity to those in Fig. 6, where the crack speed is also less than the smaller of the two Rayleigh wave speeds.

Lambros and Rosakis [12] have proposed an interface crack growth criterion based on a constant shear displacement to opening displacement ratio behind the crack tip. Therefore, the ratio of the opening displacement jump to shear displacement jump, Δ_n/Δ_t, was computed at

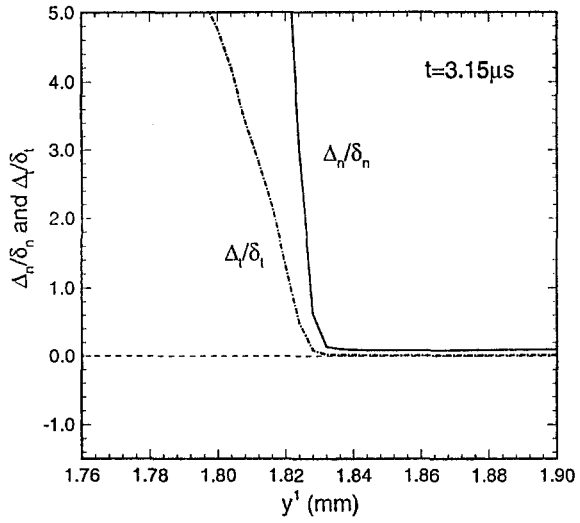

Fig. 20. Normal and tangential components of the displacement jump across the bond line near the current crack tip for (a) PMMA/MB (boundary loading on the PMMA side) at $t = 3.15$ μs, $a = 1.798$ mm and $\dot{a} = 976$ m/s and (b) PMMA/MC (boundary loading on the PMMA side) at $t = 3.2$ μs, $a = 1.676$ mm and $\dot{a} = 935$ m/s.

several times and at several locations behind the crack tip for the case shown in Figs. 22 and 23. The qualitative shape of the opening mode plots are like the one in Fig. 5(a) for the entire time interval computed (the crack speed remains less than the smaller Rayleigh wave speed, Fig. 22(a)). To illustrate typical variations, Δ_n/Δ_t at 0.1 mm behind the current crack tip is 23.4 at $t = 1.0$ μs, 14.3 at $t = 1.6$ μs and 12.5 at $t = 2.0$ μs. At 0.2 mm behind the current crack tip Δ_n/Δ_t is 45.6, 25.0 and 20.9 at these three times. The corresponding crack speeds are 719 m/s, 660 m/s and 605 m/s at $t = 1.0$ μs, $t = 1.6$ μs and $t = 2.0$ μs, respectively. The values of Δ_n/Δ_t are fairly close at the last two times, but so are the crack speeds. At earlier times Δ_n/Δ_t can vary substantially from the above values, but this may be due to the

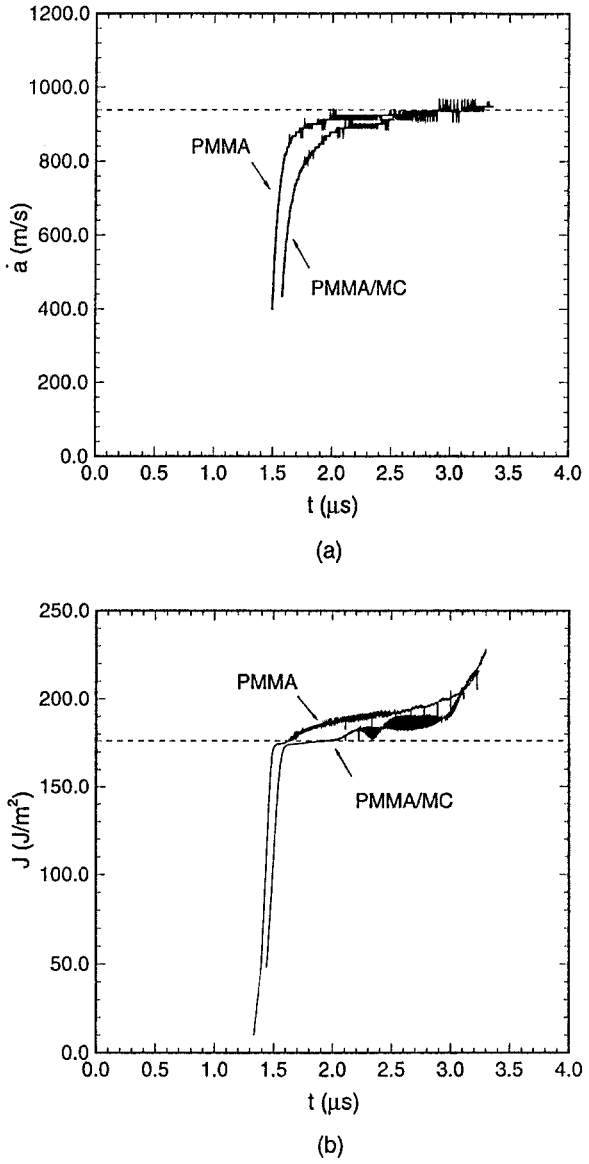

Fig. 21. Crack speed, $\dot{a}$, versus time, t, (a) and J-integral versus time (b) for an interface crack in PMMA/MC (boundary loading on the PMMA side) with V_1 =15 m/s. For comparison purposes results are also shown for homogeneous PMMA with V_1 = 30 m/s. In (a) the dashed line indicates the Rayleigh wave speed of PMMA (the Rayleigh wave speed of material C is the same as that of PMMA) and in (b) the dashed line corresponds to $J = \phi_n$.

proximity of the crack face loading region. Also, when Δ_n/Δ_t is slowly varying so is the mode mixity of the crack tip stress field.

4. Discussion

Dynamic interface crack growth has been analyzed using a framework where the crack growth history is a direct outcome of the analysis, determined by the cohesive properties along the bond line, by the properties of the materials on either side of the bond line and by the imposed

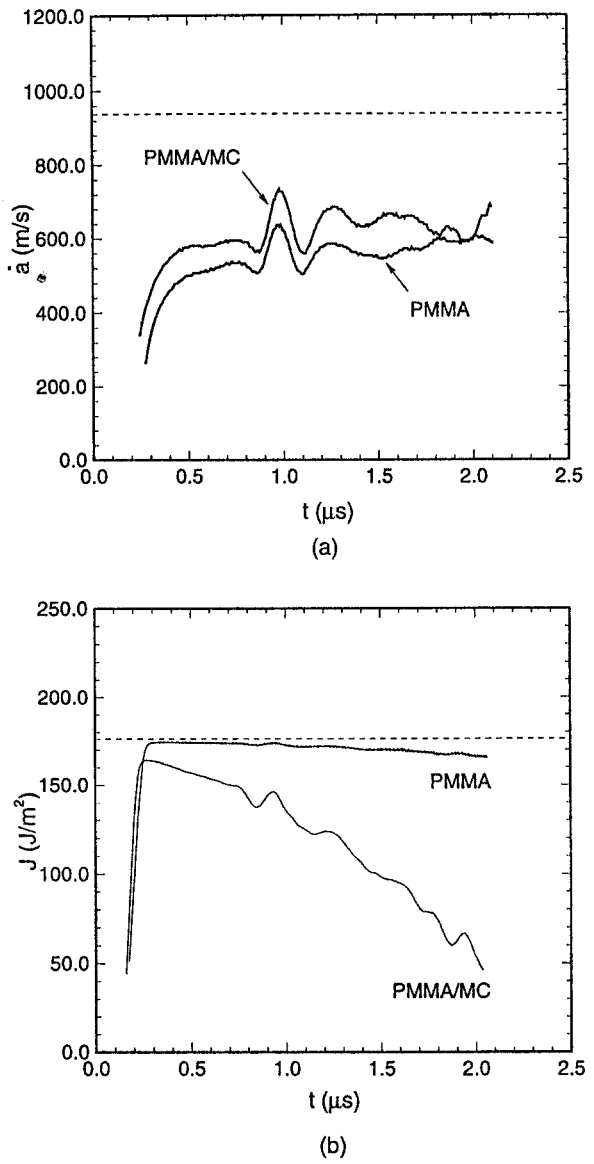

Fig. 22. Crack speed, $\dot{a}$, versus time, t, (a) and J-integral versus time (b) for an interface crack in PMMA/MC with crack face loading velocity V_1 =30 m/s. For comparison purposes results are also shown for homogeneous PMMA with $V_1 = 30$ m/s. In (a) the dashed line indicates the Rayleigh wave speed of PMMA (the Rayleigh wave speed of material C is the same as that of PMMA) and in (b) the dashed line corresponds to $J = \phi_n$.

loading. In the calculations here, the crack is constrained to grow along the bond line and the cohesive properties are fixed. Furthermore, regardless of the mode of separation (tensile or shear), the work of separation is 176.2 J/m^2. Nevertheless, the time history of J, (20), varies considerably depending on the mode of loading and on the elastic property and wave speed mismatch across the interface.

The identification of J with the energy release rate for transient crack growth requires several conditions, in addition to having a square root singularity, to be met, including; (i) that the size of the region over which cohesive surface separation occurs is small compared to

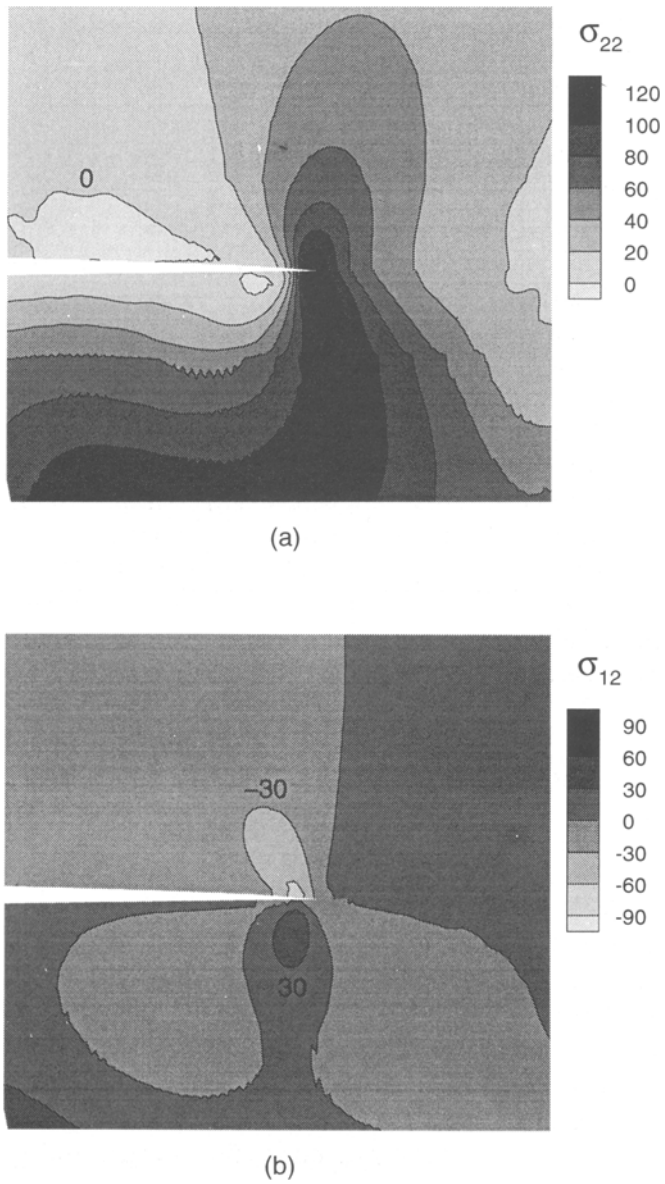

Fig. 23. Contours of physical components of Cauchy stress at $t = 1.8$ μs ($a = 1.206$ mm and $\dot{a} = 615$ m/s) for an interface crack in PMMA/MC with crack face loading velocity $V_1 = 30$ m/s. The upper half of the specimen is PMMA and the lower half is material C. The extent of the region shown is 0.25 mm in the y^1-direction and 0.23 mm in the y^2-direction. (a) Axial component σ_{22}. (b) Shear component σ_{12}.

specimen dimensions, Rice [28], and (ii) that both the $\partial(\ )/\partial t$ and the transport $(\dot{a}\partial(\ )/\partial y^1)$ contributions to the change in field quantities near the crack tip are of the same order, Nakamura et al. [29]. These conditions for J in (20) to equal the energy release rate and, hence, the work of separation are not necessarily fulfilled in the present computations.

The values of J reported are taken on contours that are outside the uniform mesh region (see Fig. 3) and thus some distance from the fracture process region. At the initiation of

crack growth, the crack along the bond line is essentially an ideal crack and in all cases J is, to a very good approximation, equal to the work of separation. During crack growth, the value of J computed on the various remote contours remains contour independent but can differ significantly from the work of separation. For example, in Fig. 12 for PMMA/MA, the value of J is much greater than the work of separation when the crack speed is greater than the smaller Rayleigh wave speed, while for MA/PMMA, with the loading on the material A side, J remains close to the work of separation during crack growth. On the other hand, for the PMMA/MC bimaterial with crack face loading, Fig. 22, J decreases substantially during crack growth. In this case, the fact that Stonely waves are available to carry energy from the process region along the cohesive surface may play a role. The present results indicate that a J versus crack speed relation for dynamic interface crack growth depends on the material mismatch and on the nature of the loading, as well as on the bond line cohesive properties.

At crack speeds less than the smaller of the two Rayleigh wave speeds, the crack tip fields show an increasing shear (mode II) component with increasing crack speed (Figs. 6, 7(a) and 8(a)), which is consistent with the analysis of Yang et al. [5], although no quantitative comparison with the asymptotic analyses has been made. Figures 7, 8, 11 and 14 show crack tip stress fields at instants where the crack speed exceeds the smaller of the two Rayleigh wave speeds (the crack speed in Fig. 14 is actually somewhat greater than the larger Rayleigh wave speed). The stress fields in these figures are quite different. However, a common feature is that the peak axial stress occurs away from the bond line. In Fig. 15, the crack speed is also larger than the smaller Rayleigh wave speed, but the peak axial stress occurs near the bond line.

Liu et al. [13] have presented asymptotic crack tip fields for an isotropic elastic solid bonded to a rigid substrate, with the crack speed above the Rayleigh wave speed of the elastic solid. Their analysis predicts no singularity for crack speeds greater than the Rayleigh wave speed but less than the shear wave speed, a singularity with exponent less than 1/2 for crack speeds greater than the shear wave speed, a crack speed range where contact occurs, and, as noted previously, infinite stress and particle velocity jumps that can occur across a singular line emanating from the crack tip. As a consequence of the order of the singularity being less than 1/2, the energy release rate is zero. In contrast, the subsonic asymptotic analysis of Yang et al. [5] gives a finite energy release rate as the smaller Rayleigh wave speed is approached from below. Hence, it is worth emphasizing that in the computations the work of separation for the cohesive surface is independent of the mode of crack opening and of the crack speed. One issue with asymptotic fields concerns their range of dominance. If the range of dominance of the asymptotic fields is not greater than the size of the fracture process region, which can be identified with the extent of the region affected by the non-zero compliance of the bond line cohesive surface, then the asymptotic fields do not govern. Of course, it is also possible that the asymptotic fields do characterize the near tip stress field, but over a length scale that is not resolved in the computations.

The calculations here have been carried out using a single finite element mesh. Xu and Needleman [19] considered the effect of mesh spacing on dynamic crack growth in homogeneous PMMA, with the crack constrained to grow along a single cohesive surface and found good agreement for the crack speeds obtained with meshes for which the node spacings in the uniform mesh region differed by a factor of 7.5. The side length of the quadrilaterals in the uniform region in Fig. 3 is $10\delta_n$, which is 1.6 times that of the finest of the meshes in [19]. However, it is possible that some of the oscillation in Fig. 14 is induced by the

numerics because of large gradients in the actual solution that cannot be resolved by the discretization.

Associated with the strong mode mixity of dynamic interface crack tip fields is contact of the crack faces, Yang et al. [5], Liu et al. [13]. In the calculations here, contact does develop in some cases (Figs. 5 and 16(a)), depending on the bimaterial combination and the imposed loading, but only when the crack speed is greater than the smaller Rayleigh wave speed. Contact occurs even when the oscillatory index ε defined in (19) is zero (Fig. 16(a)) and the size of the contact region is much larger than the cohesive surface characteristic length. There is a change in sign of the normal traction across the bond line when contact occurs. However, the periodic oscillation associated with the singular fields (at crack speeds less than the smaller Rayleigh wave speed) is not seen in the numerical results.

An issue of some controversy, see e.g. Atkinson [34], Willis [6] and Yang et al. [5], has been whether or not the interface crack speed can exceed the smaller of the Rayleigh wave speeds of the bimaterial constituents. The experimental observations of Liu et al. [8] and Lambros and Rosakis [11] show that the crack speed can exceed the smaller of the two Rayleigh wave speeds. Although the loading conditions and the material properties in the computations here differ from those in the experiments of Liu et al. [8] and Lambros and Rosakis [11], the qualitative features of the numerical results for the crack speed history and the evolution of the near tip fields are remarkably consistent with the general trends found experimentally. Additionally, the simulations explore a broader range of property mismatch conditions than are, at least readily, accessible experimentally. It is interesting to note that the fastest crack speed found is approximately the greater of the two Rayleigh wave speeds (Fig. 12(a)). It may well be that this serves as a limiting speed for an ideal interface crack because it is the fastest speed at which surface displacements can propagate on one of the crack surfaces. The crack speed in Fig. 12(a) exceeds the greater Rayleigh wave speed, perhaps because of the finite stiffness of the bond line cohesive surface, which leads to 'lift-off' as discussed in [19].

For the PMMA/Al bimaterial, the crack speeds are greater than for the corresponding homogeneous PMMA specimen (Figs 4(a) and 9(a)), as is the case for the PMMA/MC bimaterial with crack face loading (Fig. 22(a)). However, whether or not the crack speeds for a bimaterial combination are greater than for a corresponding homogeneous situation depends on the material mismatch and loading conditions (Fig. 17(a)). For a given bimaterial combination, subject to boundary loading, the resulting crack speed for a given stress amplitude, depends strongly on whether the loading is on the side with the smaller or larger Rayleigh wave speed. In Fig. 12, for PMMA/MA, the crack speed is much greater than the smaller of the two Rayleigh wave speeds and for MA/PMMA, there is a jump from one crack speed plateau to another with the arrival of a loading wave. Lambros and Rosakis [12] and Liu et al. [13] have suggested the possibility that there is an unfavorable range of crack speed greater than the smaller Rayleigh wave speed over which steady crack growth is not likely to occur due to crack face contact. Here, contact in the vicinity of the crack tip is found at crack speeds that are both much larger than (Fig. 16(a)) and slightly larger than (Fig. 5) the smaller Rayleigh wave speed.

There is interest in formulating simple phenomenological criteria for dynamic interface crack growth. Lo et al. [9] used a mode mixity and crack speed dependent critical energy release rate characterization of crack growth, while Lambros and Rosakis [12] have suggested an interface crack growth criterion based on a constant shear displacement to opening displacement ratio behind the crack tip. The present calculations (see Fig. 5 and the discussion of the PMMA/MC bimaterial subject to crack face loading) do not support the notion of a

self-similar opening profile. When the crack speed is less than the smaller Rayleigh wave speed, there can be a time range over which the ratio Δ_n/Δ_t at a given location changes slowly, but the present computations do not support this as a general criterion. The results here also show that even with a crack speed and phase angle independent characterization of the bond line cohesive properties (14), the evolution of remote crack parameters, such as J in (20), may be specimen dependent.

In fact, it would seem that a phenomenological criterion for dynamic interface crack growth would depend on whether or not large scale contact occurs near the crack tip. The present computations indicate that whether or not this takes place depends on the nature of the loading as well as on the bimaterial mismatch. Hence, general possibilities for crack speed histories may not be revealed in studies of a single loading mode. However, in all computations crack growth initiates when J equals the work of separation and, from the point of view of applications, the characterization of crack initiation in brittle solids is undoubtedly of primary importance. For crack growth, a cohesive surface description as used here seems capable of describing a broad range of phenomena characteristic of dynamic interfacial crack growth in brittle solids.

Acknowledgments

Much of this work was carried out while X.-P. Xu was a Graduate Research Assistant at Brown University supported by the Office of Naval Research through grant N00014-89-J-3054. A.N. gratefully acknowledges support from the Air Force Office of Scientific Research under Grant F49620-94-1-0300. The computations reported here were carried out on the Cray C90 computer at the San Diego Supercomputing Center. We are grateful to Professor L.B. Freund of Brown University and A.J. Rosakis of Caltech for helpful comments.

References

1. J.R. Rice, *Journal of Applied Mechanics* 55 (1988) 98–103.
2. C.F. Shih, *Materials Science and Engineering* A143 (1991) 77–90.
3. J.W. Hutchinson and Z. Suo, *Advances in Applied Mechanics* 29 (1992) 69–191.
4. L.B. Freund, *Dynamic Fracture Mechanics*, Cambridge University Press, Cambridge (1990).
5. W. Yang, Z. Suo and C.F. Shih, *Proceedings of the Royal Society of London* A433 (1991) 679–697.
6. J.R. Willis, *Philosophical Transactions of the Royal Society (London)* 274 (1973) 435–491.
7. L.M. Brock and J.D. Achenbach, *International Journal of Solids and Structures* 9 (1973) 53–67.
8. C. Liu, J. Lambros and A.J. Rosakis, *Journal of the Mechanics and Physics of Solids* 41 (1993) 1887–1954.
9. C.Y. Lo, T. Nakamura and A. Kushner, *International Journal of Solids and Structures* 31 (1994) 145–168.
10. H.V. Tippur and A.J. Rosakis, *Experimental Mechanics* 31 (1991) 243–251.
11. J. Lambros and A.J. Rosakis, *Journal of the Mechanics and Physics of Solids* 43 (1995) 169–188.
12. J. Lambros and A.J. Rosakis, *International Journal of Solids and Structures* 32 (1995) 2677–2702.
13. C. Liu, Y. Huang and A.J. Rosakis, *Journal of the Mechanics and Physics of Solids* 43 (1995) 189–206.
14. A. Needleman, *Journal of Applied Mechanics* 54 (1987) 525–531.
15. A. Needleman, *International Journal of Fracture* 42 (1990) 21–40.
16. A. Needleman, *Journal of the Mechanics and Physics of Solids* 38 (1990) 289–324.
17. V. Tvergaard and J.W. Hutchinson, *Journal of the Mechanics and Physics of Solids* 40 (1992) 1377–1392.
18. V. Tvergaard and J.W. Hutchinson, *Journal of the Mechanics and Physics of Solids* 41 (1993) 1119–1135.
19. X.-P. Xu and A. Needleman, *Journal of the Mechanics and Physics of Solids* 42 (1994) 1397–1434.
20. X.-P. Xu and A. Needleman, in *Fracture and Damage in Quasibrittle Structures: Experiment, Modeling and Computer Analysis*, Z.P. Bazant, Z. Bitnar, M. Jirasek and J. Mazars (eds.), E. and F.N. Spon, London (1994) 373–386.
21. X.-P. Xu and A. Needleman, *International Journal of Fracture* 74 (1995) 253–275.
22. X.-P. Xu and A. Needleman, in *Dislocations 93, Solid State Phenomena, 35–36*, J. Rabier, A. George, Y. Brechet and L. Kubin (eds.), Scitec Publications, Zug, Switzerland (1994) 287–302.

23. X.-P. Xu and A. Needleman, *Modelling and Simulation in Materials Science and Engineering* 1 (1993) 111–132.
24. J. Dundurs, *Journal of Applied Mechanics* 36 (1969) 650–652.
25. A.H. England, *Journal of Applied Mechanics* 32 (1965) 400–402.
26. F. Erdogan, *Journal of Applied Mechanics* 32 (1965) 403–410.
27. J.R. Rice and G.C. Sih, *Journal of Applied Mechanics* 32 (1965) 418–423.
28. J.R. Rice, *Journal of Applied Mechanics* 35 (1968) 379–386.
29. T. Nakamura, C.F. Shih and L.B. Freund, *International Journal of Fracture* 27 (1985) 229–243.
30. R.D. Krieg and S.W. Key, *International Journal of Numerical Methods in Engineering* 7 (1973) 273–286.
31. T. Belytschko, R.L. Chiapetta and H.D. Bartel, *International Journal for Numerical Methods in Engineering* 10 (1976) 579–596.
32. K.M. Liechti and Y.S. Chai, *Journal of Applied Mechanics* 59 (1992) 295–304.
33. J.D. Achenbach, *Wave Propagation in Elastic Solids*, North-Holland (1973).
34. C. Atkinson, in *Mechanics of Fracture–4: Elastodynamic Crack Problems*, G.C. Sih (ed.), Leyden, Noordhoff (1977) 213–248.